The Astrophysical Journal, 745:73 (22pp), 2012 January 20 doi:10.1088/0004-637X/745/1/73

HIGH-RESOLUTION SIMULATIONS OF CONVECTION PRECEDING IGNITION IN TYPE Ia SUPERNOVAE USING ADAPTIVE MESH REFINEMENT

A. Nonaka[1], A. J. Aspden[1,2], M. Zingale[3], A. S. Almgren[1], J. B. Bell[1], and S. E. Woosley[4]
[1] Center for Computational Sciences and Engineering, Lawrence Berkeley National Laboratory, Berkeley, CA 94720, USA
[2] School of Engineering, University of Portsmouth, Portsmouth, Hants, PO1 3DJ, UK
[3] Department of Physics & Astronomy, Stony Brook University, Stony Brook, NY 11794-3800, USA
[4] Department of Astronomy & Astrophysics, The University of California, Santa Cruz, CA 95064, USA
Received 2011 August 4; accepted 2011 October 20; published 2011 December 29

ABSTRACT

We extend our previous three-dimensional, full-star simulations of the final hours of convection preceding ignition in Type Ia supernovae to higher resolution using the adaptive mesh refinement capability of our low Mach number code, MAESTRO. We report the statistics of the ignition of the first flame at an effective 4.34 km resolution and general flow field properties at an effective 2.17 km resolution. We find that off-center ignition is likely, with radius of 50 km most favored and a likely range of 40–75 km. This is consistent with our previous coarser (8.68 km resolution) simulations, implying that we have achieved sufficient resolution in our determination of likely ignition radii. The dynamics of the last few hot spots preceding ignition suggest that a multiple ignition scenario is not likely. With improved resolution, we can more clearly see the general flow pattern in the convective region, characterized by a strong outward plume with a lower speed recirculation. We show that the convective core is turbulent with a Kolmogorov spectrum and has a lower turbulent intensity and larger integral length scale than previously thought (on the order of 16 km s^{-1} and 200 km, respectively), and we discuss the potential consequences for the first flames.

Key words: convection – hydrodynamics – methods: numerical – nuclear reactions, nucleosynthesis, abundances – supernovae: general – white dwarfs

Online-only material: color figures

1. INTRODUCTION

For the Chandrasekhar mass white dwarf (single-degenerate) progenitor model of Type Ia supernovae (SNe Ia), the location of the first flames greatly affects the outcome of the explosion (see, for example, Niemeyer et al. 1996; Plewa et al. 2004; Livne et al. 2005; García-Senz & Bravo 2005). The convective state leading up to ignition is highly nonlinear and the ignition results from a hot temperature perturbation near the center of the white dwarf. Once the temperature exceeds $\sim 8 \times 10^8$ K, a hot spot burns faster than it can cool via expansion (Nomoto et al. 1984), igniting a flame. In earlier studies on white dwarf convection in SNe Ia (Zingale et al. 2009, henceforth Z09; Zingale et al. 2011, henceforth Z11), we performed three-dimensional, full-star simulations of the final ∼3 hr of convection in a white dwarf leading up to the ignition of the first flames. We followed the nonlinear rise in the temperature approaching ignition and showed that the ignition is likely to take place off-center (50 km is most favored, with a likely range of 40–75 km, and an outer limit of 100 km) in an outward flowing parcel of fluid. Our results differed from the two-dimensional wedge simulation of Höflich & Stein (2002), who argued that the ignition is closer to the center (∼30 km) and is driven by inflow compression.

It is important to understand how robust our results for the likely ignition radius are to the resolution. With the recently implemented adaptive mesh refinement (AMR) capability in our low Mach number code, MAESTRO (Nonaka et al. 2010, henceforth N10), we are now able to study the final minutes of convection up to ignition at unprecedented resolution. We are also interested in the likelihood of multiple ignition points. Detailed visualizations of the evolution of the last few hot spots preceding ignition will be used to examine this scenario. Previous studies with an anelastic code showed that a dipole flow dominates the flow (Kuhlen et al. 2006; also seen in the follow-up studies shown in Woosley et al. 2007 and Ma 2011). Our results for non-rotating white dwarfs also show this feature. Here we examine this structure at higher resolution.

Higher resolution is also important for resolving the turbulence and capturing the turbulent cascade. Simulations have shown that the flame needs to accelerate considerably beyond its laminar value for the resulting energetics to match observations. The primary mechanism for this acceleration is thought to be instabilities and the interaction with turbulence (Mueller & Arnett 1986; Livne 1993; Khokhlov 1995; Niemeyer & Hillebrandt 1995; Niemeyer & Woosley 1997). A popular view is that the flame interacts with turbulence generated by the flame itself via instabilities. The vast majority of simulations to date have only considered this flame-generated turbulence during the explosion phase. Aspden et al. (2011) suggested that turbulent entrainment was the dominant mechanism for enhancing the burning rate, and that the local flame speed, whether laminar or turbulent, was largely unimportant. As the flame encounters lower densities and broadens, the turbulence may be able to directly affect the flame structure (at this point, the flame is said to be in the "distributed burning regime"). The altering of the flame by turbulence has been the subject of many studies, both semianalytic and one-dimensional calculations with a model for turbulence (Lisewski et al. 2000; Pan et al. 2008; Woosley et al. 2009) and multi-dimensional numerical simulations (Röpke et al. 2004; Aspden et al. 2008a, 2010, 2011). If the conditions are right, the flame may transition to a detonation in this regime (Khokhlov et al. 1997; Niemeyer & Woosley 1997; Woosley et al. 2009, 2011).

What are not well known are the characteristics of the turbulence that already exists at ignition from the centuries-long convective period. The very first flame(s) that ignite will

form flame "bubbles" that buoyantly rise away from the center as they burn outward. These bubbles will deform due to shear instabilities and interact with the pre-existing turbulence and wrinkle (Garcia-Senz & Woosley 1995; Bychkov & Liberman 1995; Iapichino et al. 2006; Zingale & Dursi 2007; Iapichino & Lesaffre 2010; Aspden et al. 2011). If the turbulence is strong enough, it could potentially disrupt the flames or even quench them. Additionally, the initial convective velocity field has been shown to introduce large asymmetries in the burning (Livne et al. 2005).

In this paper, we expand upon our previous studies of the final hours of convection leading up to the ignition of the first flames in SNe Ia. In Z09, we used 13.2 km resolution; in Z11, we used 8.68 km resolution. Here, we use the AMR capability of MAESTRO to compute ignition statistics at 4.34 km resolution and general flow field properties at 2.17 km resolution.

This paper is organized as follows. In Section 2, we give an overview of the MAESTRO algorithm, including our latest improvements for both regridding and adding an additional level of refinement to a simulation in progress. In Section 3, we describe our new high-resolution simulations. We examine the ignition statistics and compare them to our previous results in order to show that we have achieved sufficient resolution in our determination of likely ignition radii. We determine the likelihood of multiple ignition points by examining the dynamics of the last few hot spots leading up to ignition. We provide visualizations of the convective flow field to gain a better understanding of the flow structure. We include a detailed analysis of the turbulent nature of the flow field and discuss the implications for the first flames. Finally, in Section 4, we summarize and conclude.

2. NUMERICAL METHODOLOGY

MAESTRO is a finite-volume, AMR hydrodynamics code for low Mach number astrophysical flows. In our low Mach number formulation, sound waves have been analytically removed, allowing for a time step based on the fluid velocity Courant–Friedrichs–Lewy (CFL) constraint rather than the sound speed CFL constraint, while retaining compressibility effects due to background stratification, reaction heating, and compositional changes. The algorithm is described in full detail in N10. We note that the low Mach number equations do not enforce that the Mach number remains small; rather, if the dynamics of the flow are such that the Mach number does remain small, then these equations are valid approximations for the evolution of the flow. Thus, MAESTRO is not suitable for post-ignition calculations, where we expect the Mach number to quickly approach or exceed unity. Also, our low Mach number approach assumes that the background state is spherical; thus, any deformation due to rotation is not accounted for in the background state.

We now summarize the algorithm and then describe the new procedures for dynamically changing the grids as well as adding an additional level of refinement to a simulation in progress. For the simulations in this paper, we begin with data from Z11, in which we computed the last ∼3 hr of convection in a non-rotating white dwarf up to the point of ignition using 8.68 km resolution (576^3 computational cells; the problem domain is 5000 km on a side) and no AMR. We expand upon this simulation by adding a level of refinement a few minutes before ignition and examining the ignition statistics for a 4.34 km (1152^3 effective grid cells) resolution simulation. Next, we will add an additional level of AMR to examine the turbulent flow field in a 2.17 km (2304^3 effective grid cells) resolution simulation. Computer allocation limits prevent us from running 2.17 km resolution simulations to ignition, even with the efficiency gains provided by AMR.

2.1. MAESTRO Overview

MAESTRO is based on the BoxLib software framework (Rendleman et al. 2000), which provides infrastructure for block-structured AMR applications, and includes linear solvers that scale to 100,000 cores on the current generation of supercomputers (see Almgren et al. 2010 for details). We use a finite-volume approach, where each computational cell stores the average value of a state variable in that cell. The domain is decomposed into a nested hierarchy of logically rectangular Cartesian grids with computational cell width Δx^ℓ in each direction (the grids at the coarsest level are associated with level index $\ell = 1$, the first level of refinement with $\ell = 2$, etc.), and a refinement ratio of two in each spatial direction. We solve a system of coupled partial differential equations containing advection and reaction terms constrained by an equation of state that takes the form of a divergence constraint on the velocity field. This constraint is enforced using a projection method, which requires linear solvers to solve a variable-coefficient Poisson equation.

One feature that makes MAESTRO different from standard AMR hydrodynamics codes is the presence of base state variables, which are functions of radius and time, (r, t), as opposed to Cartesian grid quantities, which are functions of all spatial dimensions and time, $(\boldsymbol{x}, t)$. We represent base state variables using a one-dimensional, time-dependent array. The base state array has a constant grid spacing, $\Delta r = \Delta x^{\ell_{\max}}/5$, where $\ell_{\max}$ is the finest level in the simulation, and due to the spherical nature of our problem does not directly align with the Cartesian grid. Figure 1 shows a depiction of the Cartesian grid, one-dimensional radial array, and a graphical representation of how they relate to each other. Some base state variables are cell-centered and others are defined on edges. Each of the base state variables is computed directly from other base state variables and/or Cartesian grid variables. The base state density obeys an evolution equation within each time step (described below). We require frequent mapping from the base state to the Cartesian grid and vice versa. In N10, we describe how we interpolate a base state quantity onto the Cartesian grid, as well as a "lateral average" procedure that determines the average value of a Cartesian grid quantity at a particular radius and maps that value onto the radial array.

In the following overview, all variables are assumed to live on the Cartesian grid, unless noted otherwise. MAESTRO solves the equations of reacting flow constrained by an equation of state in the form of a divergence constraint. The species are evolved according to

$$\frac{\partial(\rho X_k)}{\partial t} = -\nabla \cdot (\rho X_k \mathbf{U}) + \rho \dot{\omega}_k, \tag{1}$$

where ρ is the density, X_k is the mass fraction of species k, $\mathbf{U}$ is the velocity field, and $\dot{\omega}_k$ is the creation rate of species k due to reactions. We note that the density can be determined at any time using

$$\rho = \sum_k (\rho X_k), \tag{2}$$

and thus density does not have to be explicitly evolved in time.

We define a base state density, $\rho_0(r, t)$, that represents the average value of density at a particular radius. The base state density has its own evolution equation, as described below. The

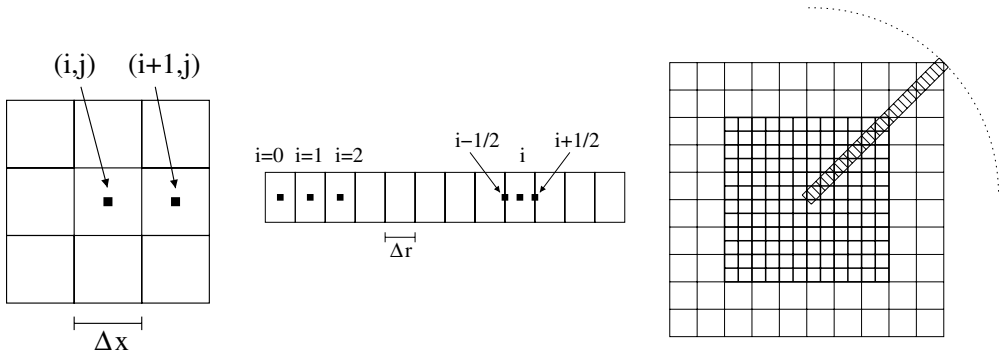

Figure 1. Left: for data on the Cartesian grid (shown here in two dimensions), we use a cell-centered convention to denote the average value over the computational cell. Center: the base state variables live on a one-dimensional radial array and can live at cell centers or edges. Right: a graphical depiction of how the base state and Cartesian grid are related. Note that there is no direct alignment between the radial cell centers and the Cartesian grid cell centers.

base state (thermodynamic) pressure, $p_0(r,t)$, is computed using the condition of hydrostatic equilibrium,

$$\nabla p_0 \equiv \frac{\partial p_0}{\partial r} = -\rho_0 g, \tag{3}$$

where the gravity, $g(r,t)$, is computed by integrating ρ_0 assuming piecewise-constant profiles of ρ_0 within each radial cell.

In general, given ρ and X_k, we could derive the temperature from the specific enthalpy, h, evolved as

$$\frac{\partial(\rho h)}{\partial t} = -\nabla\cdot(\rho h\mathbf{U}) + \frac{Dp_0}{Dt} + \rho H_{\rm nuc}, \tag{4}$$

where $H_{\rm nuc}$ is the energy generation rate from reactions. In practice, we adopt the prescription used in Z09 and Z11 and derive the temperature from ρ, X_k, and p_0, effectively decoupling the enthalpy from the problem. In the future, we will seek ways to evolve the enthalpy in a manner that minimizes the drift from the equation of state.

The velocity field is evolved according to

$$\frac{\partial\mathbf{U}}{\partial t} = -\mathbf{U}\cdot\nabla\mathbf{U} - \frac{1}{\rho}\nabla\pi - \frac{\rho-\rho_0}{\rho}g\boldsymbol{e}_r, \tag{5}$$

where π is the perturbational pressure, i.e., the local deviation of the total pressure from p_0, and $\boldsymbol{e}_r$ is the unit vector in the outward radial direction. The evolution of the thermodynamic variables (ρ, X_k, and p_0) is constrained by the equation of state, which we represent as a divergence constraint on the velocity field,

$$\nabla\cdot(\beta_0\mathbf{U}) = \beta_0\left(S - \frac{1}{\overline{\Gamma_1}p_0}\frac{\partial p_0}{\partial t}\right). \tag{6}$$

Here, $\beta_0(r,t)$ is a base state quantity that captures the expansion/contraction of a fluid parcel as it changes altitude, and S is a local source term that captures the compressibility effects due to reactions and compositional changes. The quantity $\overline{\Gamma_1}(r,t)$ is a base state variable representing the average at constant radius of $\Gamma_1 = \partial\log p/\partial\log\rho|_s$, where s is the entropy. A full derivation of this constraint, the form of β_0 and S, and the numerical projection can be found in Almgren et al. (2006a, 2006b, 2008).

The evolution equation for ρ_0 is

$$\frac{\partial\rho_0}{\partial t} = -\frac{\partial(\rho_0 w_0)}{\partial r} - \frac{\partial\eta_\rho}{\partial r}, \tag{7}$$

where $w_0(r,t)$ is the base state expansion velocity, which accounts for the expansion of the atmosphere due to large-scale heating. We compute this term by integrating a one-dimensional version of the divergence constraint (Equation (6)). The quantity $\eta_\rho(r,t)$ is a base state quantity that accounts for changes in background stratification due to large-scale convection (see Almgren et al. 2008 and N10).

The velocity field can be decomposed into the base state velocity and a local velocity, $\widetilde{\mathbf{U}}(\boldsymbol{x},t)$, that governs the local dynamics,

$$\mathbf{U}(\boldsymbol{x},t) = w_0(r,t)\boldsymbol{e}_r + \widetilde{\mathbf{U}}(\boldsymbol{x},t). \tag{8}$$

We follow the approach in N10, where we compute the evolution of these terms separately, and thus evolve $\widetilde{\mathbf{U}}$ subject to a perturbational form of Equations (5) and (6).

We note that the base state quantities ρ_0, p_0, β_0, $\overline{\Gamma_1}$, and η_ρ are stored on radial cell centers, whereas w_0 is stored at radial edges.

To summarize, we advance Equations (1), (5), and (7) subject to Equations (2), (3), and (6). We use a second-order predictor–corrector approach in which we discretize the advection terms using an unsplit Godunov method, compute the effect of reactions on a cell-by-cell basis using the VODE stiff ODE package (Brown et al. 1989), and couple these processes using Strang splitting. We enforce the divergence constraint on velocity using a projection method, which uses multigrid to solve a variable-coefficient Poisson equation for the update of the perturbational pressure, π.

2.2. Regridding and Adding a Level of Refinement

Regridding is the process of redefining the AMR grid structure based on user-specified refinement criteria. The regridding algorithm also uses interpolation stencils to initialize data on newly created refined grids from underlying coarse data. Here we have improved the regridding algorithm described in N10 and have also implemented a new algorithm for adding an additional level of refinement to a simulation in progress. Our approach to AMR uses a nested hierarchy of logically rectangular grids with successively finer grids at higher levels. This is based on the strategy introduced for gas dynamics by Berger & Colella (1989), extended to the incompressible Navier–Stokes equations by Almgren et al. (1998), and extended to low Mach number reacting flows by Pember et al. (1998) and Day & Bell (2000). We refer the reader to these works for more details. The complication in applying these methods to MAESTRO is the presence of the time-dependent base state variables. We refer the reader to N10 for the MAESTRO-specific implementation including

details on creating and managing the grid hierarchy, communication between levels, and the implementation of AMR with time-dependent base state variables.

We note an error in the Cartesian grid regridding procedure as described in Section 5.1 of N10. For problems with three or more total AMR levels, we require that each grid at level $\ell + 1$ be a distance of at least four (not two as previously reported) level ℓ cells from the boundary between level ℓ and level $\ell - 1$ grids; this allows us to always fill "ghost cells" at level $\ell + 1$ from the level ℓ data (or the physical boundary conditions, if appropriate).

The major change regarding the regridding of the Cartesian grid data is in the way we interpolate coarse data to fill newly created fine grids. Our piecewise-linear interpolation algorithm applied to ρX_k causes an artificial buoyancy term to appear in the momentum equation, leading to spurious velocities emanating from the coarse–fine interface. The basic idea of the improved algorithm is to interpolate ρ' and X_k separately, rather than ρX_k, to initialize data on the newly created refined grids.

The variables on the Cartesian grid that we need to interpolate are $\mathbf{U}$, ρ, ρX_k, $\nabla\pi$, and S. The base state does not change structure, but we still need to recompute ρ_0, p_0, β_0, and $\overline{\Gamma_1}$ to be consistent with the data on the Cartesian grid. We keep the original values of w_0 and η_ρ. Here are the steps for regridding.

1. Starting with level 1 and user-defined refinement criteria, tag all level 1 Cartesian cells that satisfy the criteria for refinement. Create the level 2 grids and initialize the level 2 data by copying from the previous grid structure where possible. Otherwise, use piecewise-linear interpolation from underlying coarse cells to initialize any newly created refined regions, including ghost cells. Continue to add additional levels of refinement in this way until all data on the grids at level $\ell_{\max}$ are filled in. There is a slight modification to the interpolation procedure for ρX_k, where we first interpolate $\rho' = \rho - \rho_0$ and $X_k = (\rho X_k)/\rho$ to newly refined regions and then construct $\rho X_k = (\rho' + \rho_0)X_k$.
2. Recompute ρ_0 by calling the lateral average routine, then use Equation (3) to compute p_0.
3. Recompute T and Γ_1 on each Cartesian cell using the equation of state. Recompute $\overline{\Gamma_1}$ by calling the lateral average routine. Then, recompute β_0 as described in N10.
4. Compute a new appropriate Δt.

The procedure for adding an additional level of refinement to a simulation in progress is largely based on the standard regridding procedure, except that now the base state array will have twice as many cells since Δr is based on the resolution of the finest Cartesian grid, i.e., $\Delta r = \Delta x^{\ell_{\max}}/5$. To add one additional level of refinement to a simulation in progress:

1. Perform step 1 in the regridding procedure defined above, except allowing for an additional level of refinement.
2. Define a new base state array with twice the resolution, i.e., $\Delta r = \Delta x^{\ell_{\max}}/5$. Call the lateral average routine to compute ρ_0 and use Equation (3) to recompute p_0.
3. Recompute T and Γ_1 on each Cartesian cell using the equation of state. Call the lateral average routine to compute $\overline{\Gamma_1}$. Then, recompute β_0 as described in N10.
4. The base state variable w_0 is edge-centered. We compute w_0 on the finer base state array using direct injection from the previous coarser base state array on aligning edges, and piecewise-linear interpolation on non-aligning edges.
5. The base state variable η_ρ is cell-centered. We interpolate η_ρ onto the finer base state array using piecewise-linear interpolation from the previous coarser base state array.[5]
6. Compute a new appropriate Δt.

3. RESULTS

We now focus on one particular simulation performed in Z11, in which we computed the last ∼3 hr of convection up to the point of ignition for a non-rotating white dwarf using 8.68 km resolution (576^3 computational cells) and no AMR. As before, we define ignition as the time when the maximum temperature exceeds 8×10^8 K. Here is a summary of our results from that simulation.

1. The plots of peak temperature, peak radial velocity, and peak Mach number as a function of time each exhibited a gradual, nonlinear rise until the peak temperature exceeded $\sim 7 \times 10^8$ K. Then, the rise in each field became much steeper, with ignition following shortly afterward.
2. The first cell to ignite was 25.7 km off-center and had an outward radial velocity of 5.1 km s^{-1}.
3. For the last ∼3 minutes preceding ignition, the average radius of the hottest cell was 52.3 km with a standard deviation of 25.5 km.
4. Histograms of the radius of the hottest cell during the final ∼3 minutes preceding ignition averaged over small time intervals indicated that
   (a) the favored ignition radius was 50 km, with a likely range of 40–75 km and an outer limit of 100 km;
   (b) nearly all of the hot spots had an outward radial velocity; and
   (c) these two results were consistent within any smaller time window within the final ∼3 minutes.
5. Visualizations of the convective flow field showed a dipole structure in the interior convectively unstable core, and a sharp boundary between the interior and the stably stratified outer portion of the star.

In this section, we examine the robustness of the ignition results at higher resolution. Then, we use new visualization techniques to follow the last few hot spots preceding ignition to determine the likelihood of multiple ignition points. We also visualize the overall convective flow field to show the detailed fine-scale structure, as well as a more coherent picture of the large-scale features. Finally, we analyze the turbulent spectrum to quantify the extent to which we have resolved the turbulent cascade and discuss the effect that turbulence could have on the first few flames.

We note that we do not consider a high-resolution rotating white dwarf at this time. A 576^3 rotating simulation developed high velocities on the surface of the star at the poles, likely due to the deformation of the star. In our lower-resolution rotating runs in Z11, we saw a similar feature, but the velocities did not become large enough to restrict our time step as they do for the higher-resolution runs. A potential future solution to this would be to reformulate the base state in MAESTRO to deal with equipotentials instead of a spherical radius.

[5] In practice, we store η_ρ on radial cell centers and edges as separate arrays. We interpolate the radial cell-centered and edge-based arrays onto the finer base state arrays separately, rather than simply interpolating the radial cell-centered array onto the finer base state array, and then arithmetically averaging to get the radial edge-centered array. In the future, we will run in the latter mode for simplicity, noting that the effects of this change are very minor and that both methods are second order.

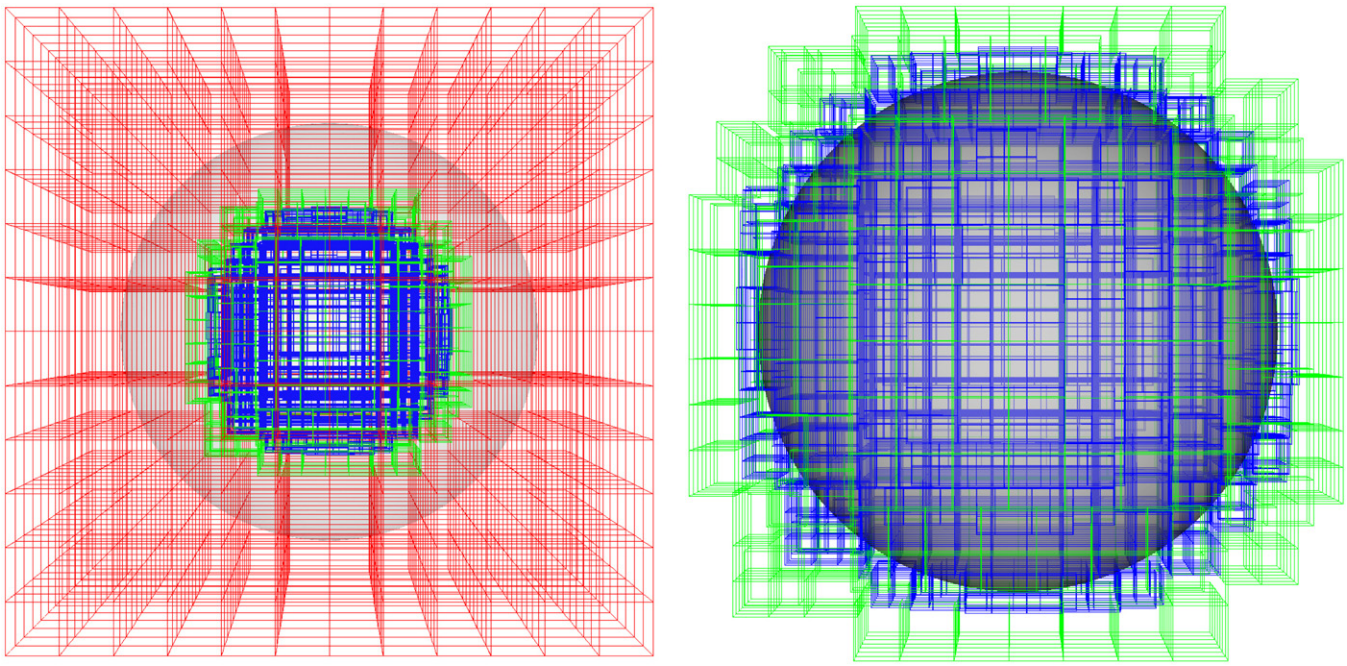

Figure 2. Grid structure for our three-level simulations. The base grid has 576^3 grid cells (8.68 km resolution), and the refined grids have effective 1152^3 (4.34 km) and 2304^3 (2.17 km) grid cells. The red, green, and blue outlines indicate boxes which can contain up to 64^3 grid cells. Left: the shaded region indicates the edge of the star, defined by the location where $\rho = 10^5$ g cm^{-3} at $r \approx 1890$ km. Right: in this zoom-in, the shaded region indicates the edge of the convective region, defined by the location where $\rho \approx 1.26 \times 10^8$ g cm^{-3} at $r \approx 1030$ km. The finest grids contain the entire convective region.

(A color version of this figure is available in the online journal.)

3.1. Problem Setup

The 8.68 km resolution simulation in Z11 followed the last ∼10,500 s preceding ignition. The simulation required ∼6 million CPU hours on the Jaguarpf Cray XT5 at Oak Ridge Leadership Computational Facility (OLCF). Assuming perfect scaling and no AMR overhead, a 4.34 km simulation from $t = 0$ would require a factor of ∼4 more computational resources (since the time step is a factor of two smaller, and with our tagging criteria we have approximately the same number of cells at levels 1 and 2, so there are twice as many total grid cells). Due to computer allocation limits, running 4.34 km resolution from $t = 0$ is infeasible, so instead we add an additional level of refinement to an 8.68 km simulation at a time corresponding to ∼250 s preceding ignition. The edge of the star lies where $\rho_0 \approx 1 \times 10^5$ g cm^{-3}, corresponding to a radius of $r \approx 1890$ km. We refine all level 1 cells where $\rho > 5 \times 10^7$ g cm^{-3} ($r \approx 1225$ km), which more than encompasses the convective region (the convective region boundary lies approximately where $\rho_0 \approx 1.26 \times 10^8$ g cm^{-3}, with $r \approx 1030$ km). This new simulation has 4.34 km resolution (1152^3 effective grid cells). We note that since this problem is highly nonlinear, we do not expect the ignition to occur at exactly the same time. In fact, the 4.34 km simulation takes ∼350 s to ignite. Approximately 100 s into the 1152^3 simulation, we add another level of refinement, tagging all level 2 cells where $\rho > 1 \times 10^8$ g cm^{-3} ($r \approx 1080$ km). This second new simulation has 2.17 km resolution (2304^3 effective grid cells). We run the 2.17 km simulation for ∼80 s and not to ignition (again due to computer allocation limits).

The resulting three-level grid structure is shown in Figure 2. The grids adaptively change as the simulation progresses, but since the overall base state density profile of the star is relatively constant (as shown in Z11), the grids do not change significantly over time. Some specific details concerning this grid structure are as follows.

1. The red grids are at 8.68 km resolution. There are 1728 red grids, each of which has 48^3 grid cells (∼191 million grid cells total).
2. The green grids are at 4.34 km resolution. There are 1736 green grids of varying sizes, with a maximum of 48^3 cells per grid. (∼141 million grid cells total).
3. The blue grids are at 2.17 km resolution. There are 3646 blue grids of varying sizes, with a maximum of 64^3 cells per grid. (∼654 million grid cells total).

By contrast, a simulation without AMR at 2.17 km resolution would contain $2304^3 = 12.2$ billion grid cells, or a factor of ∼12 more grid cells than the AMR simulation.

For the simulations in this paper, we use the recently implemented hierarchical approach to parallelism described in Almgren et al. (2010). We use a coarse-grain parallelization strategy to distribute grids to nodes, where the nodes communicate with each other using standard Message Passing Interface (MPI). We also use a fine-grain parallelization strategy in the physics-based modules and the linear solvers, in which we use OpenMP to spawn a thread on each core on a node. Each thread operates on a portion of the associated grid. Grids at each level of refinement are distributed independently. This approach allows for MAESTRO (in particular the linear solvers) to scale to ∼100,000 cores. All simulations were performed on the Jaguarpf Cray XT5 at OLCF using 1728 MPI processes with six threads per MPI process (10,368 total cores).

3.2. General Behavior

We begin by reproducing some of the diagnostics used in Z11 using data from the 4.34 km and 2.17 km simulations. In

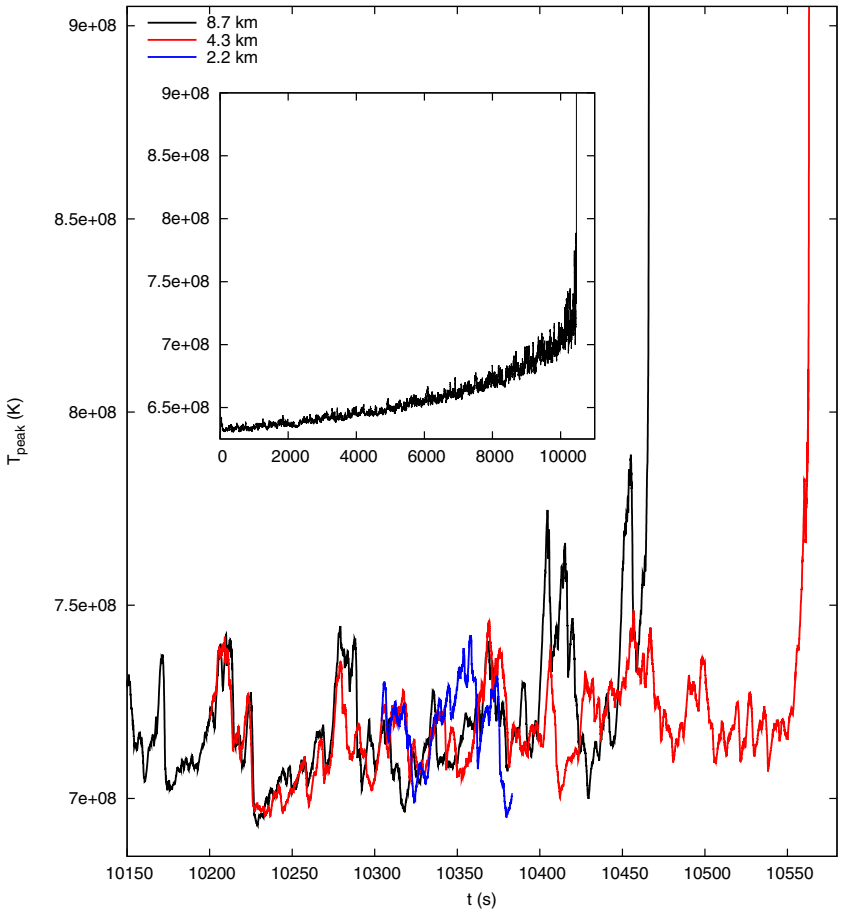

Figure 3. Peak temperature leading up to ignition for the 8.68 km, 4.34 km, and 2.17 km simulations. The inset plot shows the long-time behavior of the 8.68 km simulation originally presented in Z11.

Figure 3, we plot the peak temperature as a function of time for the 4.34 km and 2.17 km resolution simulations, and also include original 8.68 km resolution data for comparison. First, we see that over the last few minutes, the temperature profiles have the same general trend. The peak temperature value steadily grows with time, including fluctuations of several percent. Once the star ignites, the peak temperature rapidly increases beyond 8×10^8 K. We consider the local temperature peaks preceding ignition to be "failed" ignition points, i.e., hot bubbles that are not quite hot enough to cause the temperature to run away. The ignition time for the 8.68 km and 4.34 km simulations differ by ∼100 s. Due to the highly nonlinear nature of this problem, this result is not particularly surprising. At the beginning of the 4.34 km simulation, we notice that the peak temperature curves track each other very well for the first ∼80 s (from time range 10,200–10,280 s) before the curves begin to show different behavior. This is not particularly surprising either since the 4.34 km solution begins as an interpolated imprint of the 8.68 km simulation. After ∼80 s, we say that the peak temperature in the 4.34 km simulation has decorrelated from the 8.68 km simulation, and we expect the statistical properties of the hot spots near the center of the star to be consistent with an independent 4.34 km simulation initialized at time $t = 0$. We still expect the general convective flow field to look qualitatively similar for a longer period of time. The 2.17 km simulation shows similar behavior; after initializing the simulation from the 4.34 km data, it takes ∼40 s for the peak temperature curves to decorrelate.

We would like to comment on the time step used in these simulations. Using an advective CFL number of 0.7, the average time steps over the time range 10,300–10,380 s are approximately 0.027 s (for the 8.68 km simulation), 0.016 s (4.34 km), and 0.010 s (2.17 km). The time steps do not quite change by a factor of two with refinement since the peak velocities do not necessarily lie in the refined convective region. We also want to comment on the efficiency of the low Mach number formulation as compared to an explicit, fully compressible approach. In Nonaka et al. (2011), we showed that the 8.68 km simulation took a time step of a factor of ∼70 larger than a compressible code, yet a low Mach number time step takes approximately 2.5 times as long given the same computational resources, yielding an overall efficiency increase of ∼28 over a compressible code. This comparison is especially meaningful because we compared to the CASTRO (Almgren et al. 2010) compressible code, which is based on the same BoxLib framework as MAESTRO, and uses the same unsplit Godunov advection formalism, same equation of state, and same reaction network ODE solver.

Next, in Figures 4 and 5 we plot the peak Mach number and peak radial velocity as a function of time. We see the same general behavior as in the 8.68 km simulation, where the peak Mach number and radial velocity remain relatively constant until the final seconds preceding ignition, where the values rapidly increase.

The next quantities of interest are the radius of the first ignited cell and its corresponding outward radial velocity. In the 4.34 km

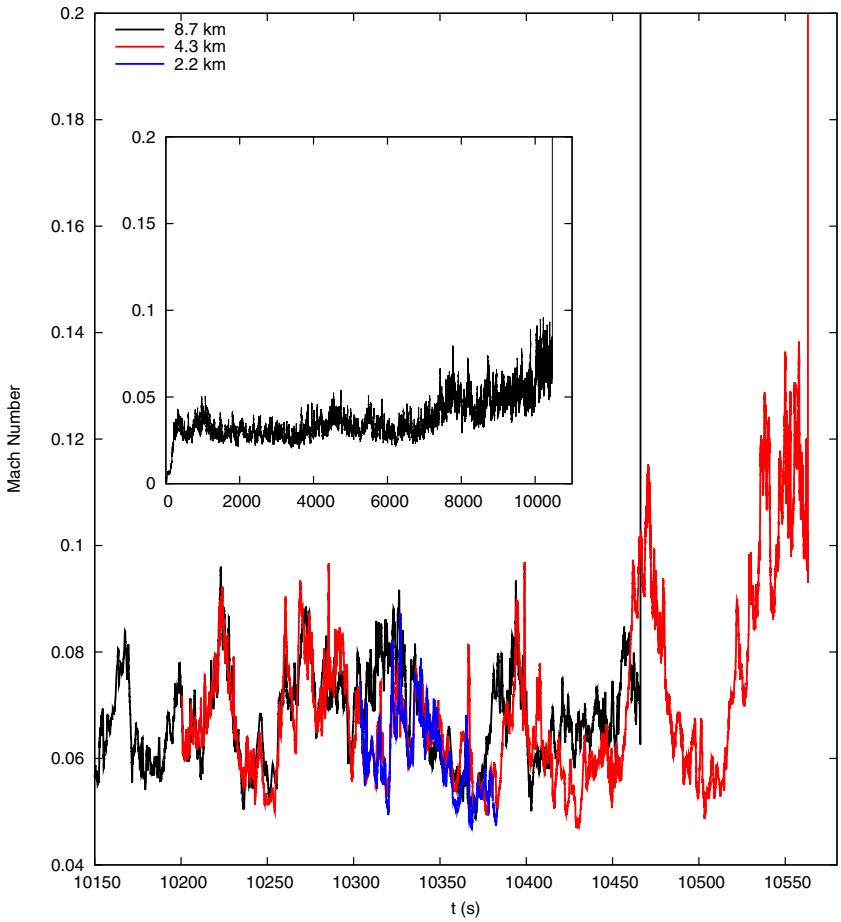

Figure 4. Peak Mach number leading up to ignition for the 8.68 km, 4.34 km, and 2.17 km simulations. The inset plot shows the long-time behavior of the 8.68 km simulation originally presented in Z11.

simulation, the radius of the ignited cell is 41.3 km, with outward radial velocity of 9.5 km s^{-1}. We compare these values to those reported in Table 1 of Z11; the 8.68 km simulation had an ignition cell radius of 25.7 km with outward radial velocity of 5.1 km s^{-1}.

We would also like to examine the ignition radius and radial velocity if we were to define ignition as 1.1×10^9 K rather than 8×10^8 K. However, by advancing the solution using our advective CFL condition, the simulation quickly becomes unphysical. Specifically, if we continue to let the white dwarf evolve past 8×10^8 K, over the next ∼0.5 s (∼60 time steps), the peak temperature steadily climbs to $\sim 9 \times 10^8$ K while the peak Mach number holds steady at ∼0.1. Then, over the next few time steps, the temperature unphysically spikes to $\sim 8 \times 10^9$ K, with the peak Mach number quickly climbing to well over 1000. Our low Mach number model has obviously broken down, so these results are not physical. To remedy this situation, and to advance our simulation to 1.1×10^9 K, we apply a heuristic time step limiter, which attempts to reduce the time step so the peak temperature does not increase by more than ∼1% each step. We limit the time step using

$$\Delta t = \min \left[\Delta t_{\rm CFL}, \frac{\Delta t_{\rm CFL}}{100} \frac{T_{\rm max}^{n-1}}{T_{\rm max}^{n} - T_{\rm max}^{n-1}} \right], \qquad (9)$$

where $\Delta t_{\rm CFL}$ is the time step computed using our standard advective CFL condition, $T_{\rm max}^{n}$ is the maximum temperature in the domain at the current time step, and $T_{\rm max}^{n-1}$ is the maximum temperature in the domain from the previous time step. In doing this, we find that that we reach 1.1×10^9 K at 0.57 s after 8×10^8 K, the ignition point has advected to a larger radius (48.9 km), and the ignition point radial velocity has increased to $v_r = 14.0$ km s^{-1}. These results are not surprising, given the ignition conditions at 8×10^8 K reported above.

In Z11 we studied the time history of the hottest cell over the last few minutes. We gathered statistics to help us in our determination of likely ignition radii and repeat the same diagnostics here. In Figure 6, we show the radius of the hottest cell as a function of time for the final seconds preceding ignition for the 4.34 km simulation. In Table 2 of Z11, we computed the average radius of the hottest zone, and its standard deviation, for the last 200 s and 100 s preceding ignition. For the 4.34 km simulation, over the last 200 s, the average hot spot radius and standard deviation are 54.0 km and 22.1 km (as compared to 52.3 km and 25.5 km for the 8.68 km simulation). Over the last 100 s, the average hot spot radius and standard deviation are 54.7 km and 22.5 km (as compared to 54.7 km and 27.3 km for the 8.68 km simulation). This tells us two things. First, the hot spot statistics do not seem to change much whether we consider the final 200 s or 100 s preceding ignition. Second, the results are very similar to the 8.68 km simulation, implying that we have sufficient resolution in our determination of likely ignition radii.

Next, as in Z11, we break the final approach to ignition into small time intervals and look at properties of the flow within each time interval. We consider the last 200 s preceding ignition, and

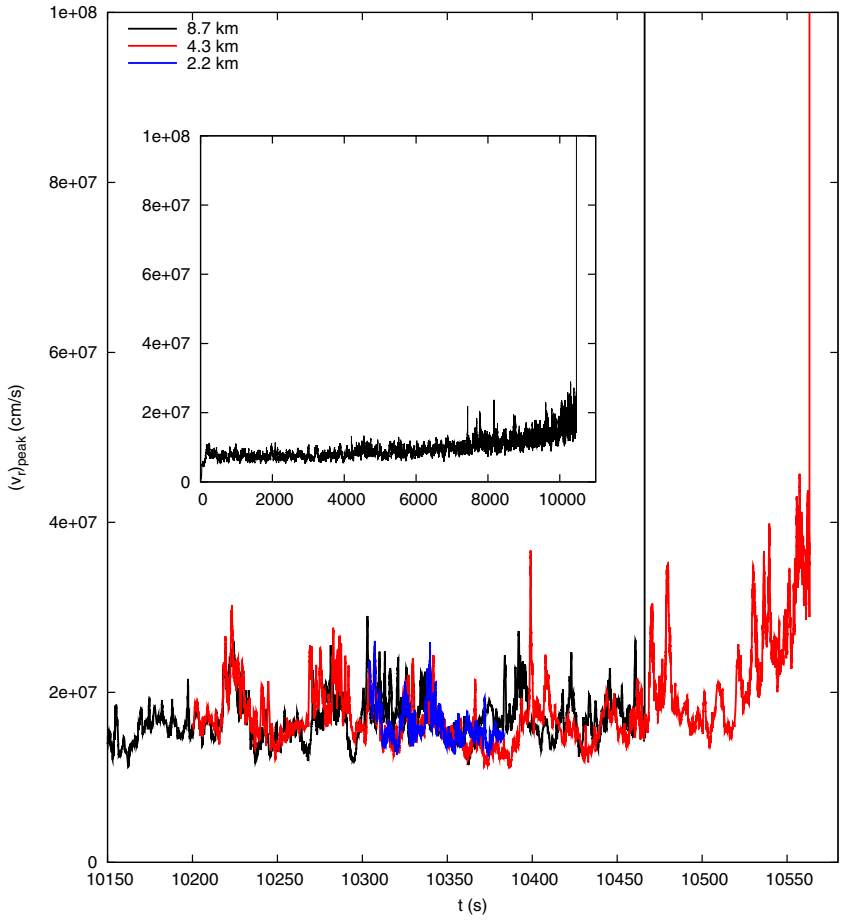

Figure 5. Peak radial velocity leading up to ignition for the 8.68 km, 4.34 km, and 2.17 km simulations. The inset plot shows the long-time behavior of the 8.68 km simulation originally presented in Z11.

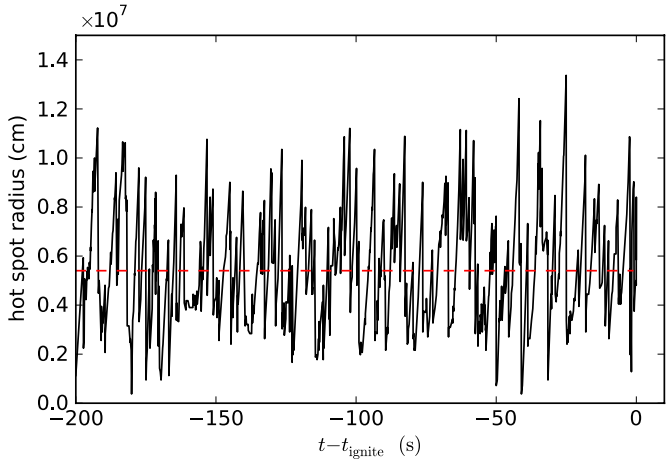

Figure 6. Radial location of the hottest cell as a function of time for the 4.34 km simulation. Only the last 200 s before ignition are shown. Here we see that right up to the end of the calculation the hot spot location changes rapidly. The horizontal dashed line indicates the average radial position of the hot spot from 200 s to 1 s before ignition.

use time intervals of $\Delta t_{\rm hist} = 1.0$ s and 0.5 s. Within each time interval, we compute the average radius of the hottest cell, the average temperature of the hottest cell, and the average radial velocity of the hottest cell. We sort this data into histograms to understand the statistics of the last few hot bubbles preceding ignition. In each of the following figures, we show histograms for both $\Delta t_{\rm hist} = 1.0$ s and 0.5 s. Figure 7 shows histograms of the hottest cell, sorted by radius, with the colors representing the average temperature of the hottest cell over the averaging interval. Figure 8 shows histograms of the hottest cell, sorted by radius, with the colors representing the average radial velocity of the hottest cell over the averaging interval. Figure 9 shows histograms of the hottest cell, sorted by radius, with the colors representing time to ignition. Overall, the results are consistent with our observations in Z11, which we now summarize. Some general observations are as follows.

1. From each set of histograms, we see that the hot spot is most likely to be found between 40 km and 75 km off-center. This is consistent with both Figure 6 and the histograms from Z11. However, we do not see the slight extended tail observed in Z11, which indicated a slight preference for the hot spots to lie at larger radii within the distribution.
2. For each set of histograms, we observe that the results are essentially the same regardless of whether $\Delta t_{\rm hist} = 1.0$ s or 0.5 s is used as the averaging interval.

Some figure-specific observations are as follows.

1. In Figure 7, within each temperature interval, the overall shape of the distribution appears roughly the same, with a peak slightly greater than 50 km, indicating that hot spots of all temperatures can appear at any radius in the distribution.
2. In Figure 8, nearly all of the hot spots have an outward radial velocity. Also, there is a tendency for the hot spots at larger

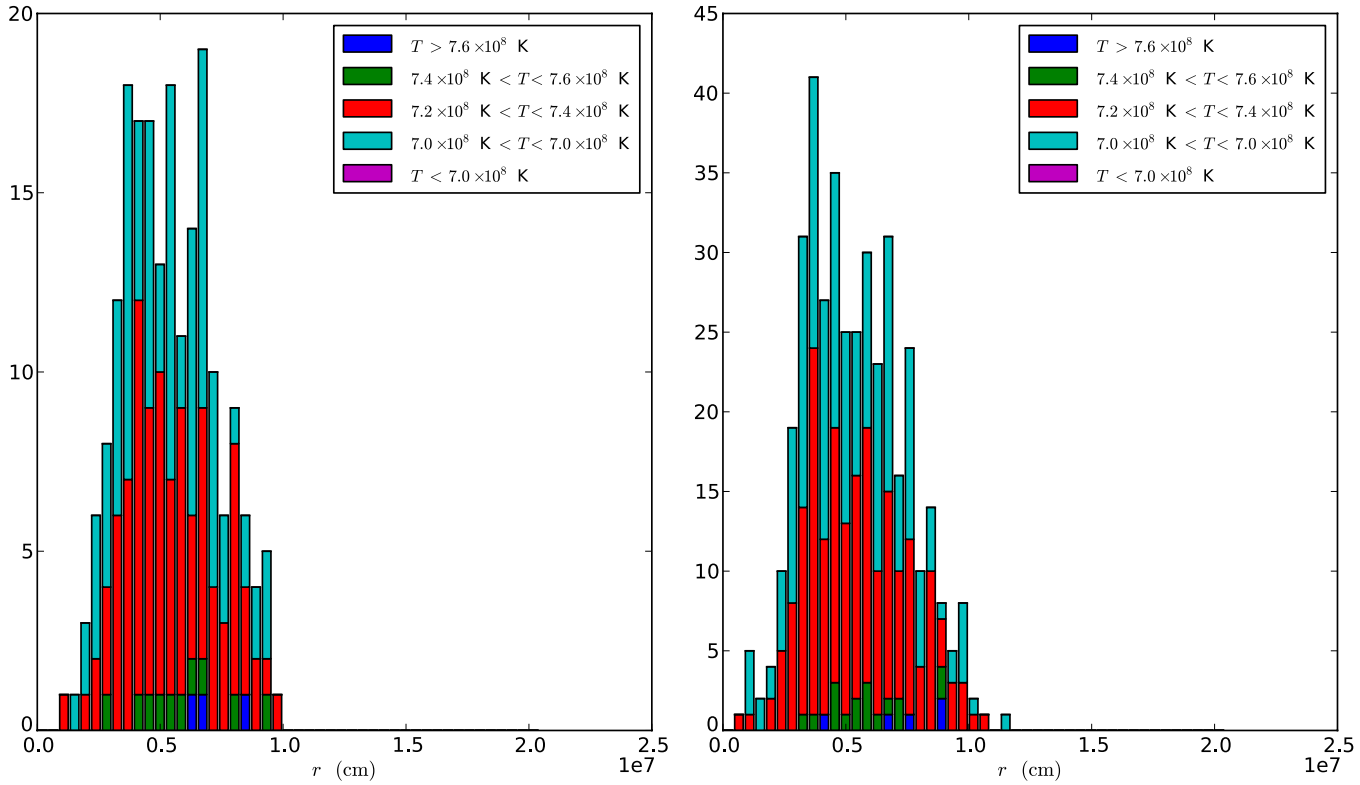

Figure 7. Histograms of the hottest cell, sorted by radius, with the colors representing the average temperature of the hottest cell over the averaging interval for the 4.34 km simulation with (left) $\Delta t_{\rm hist} = 1.0$ s and (right) $\Delta t_{\rm hist} = 0.5$ s.

(A color version of this figure is available in the online journal.)

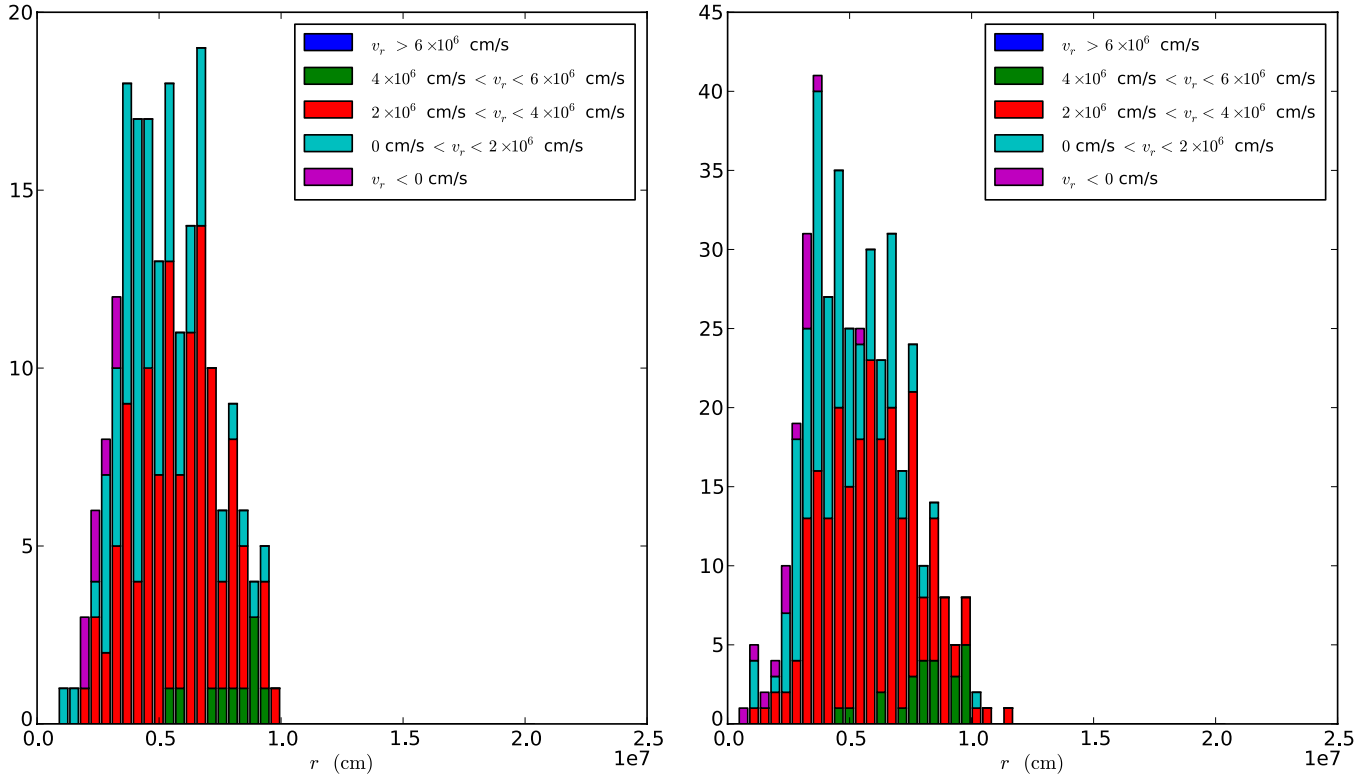

Figure 8. Histograms of the hottest cell, sorted by radius, with the colors representing the average radial velocity of the hottest cell over the averaging interval for the 4.34 km simulation with (left) $\Delta t_{\rm hist} = 1.0$ s and (right) $\Delta t_{\rm hist} = 0.5$ s.

(A color version of this figure is available in the online journal.)

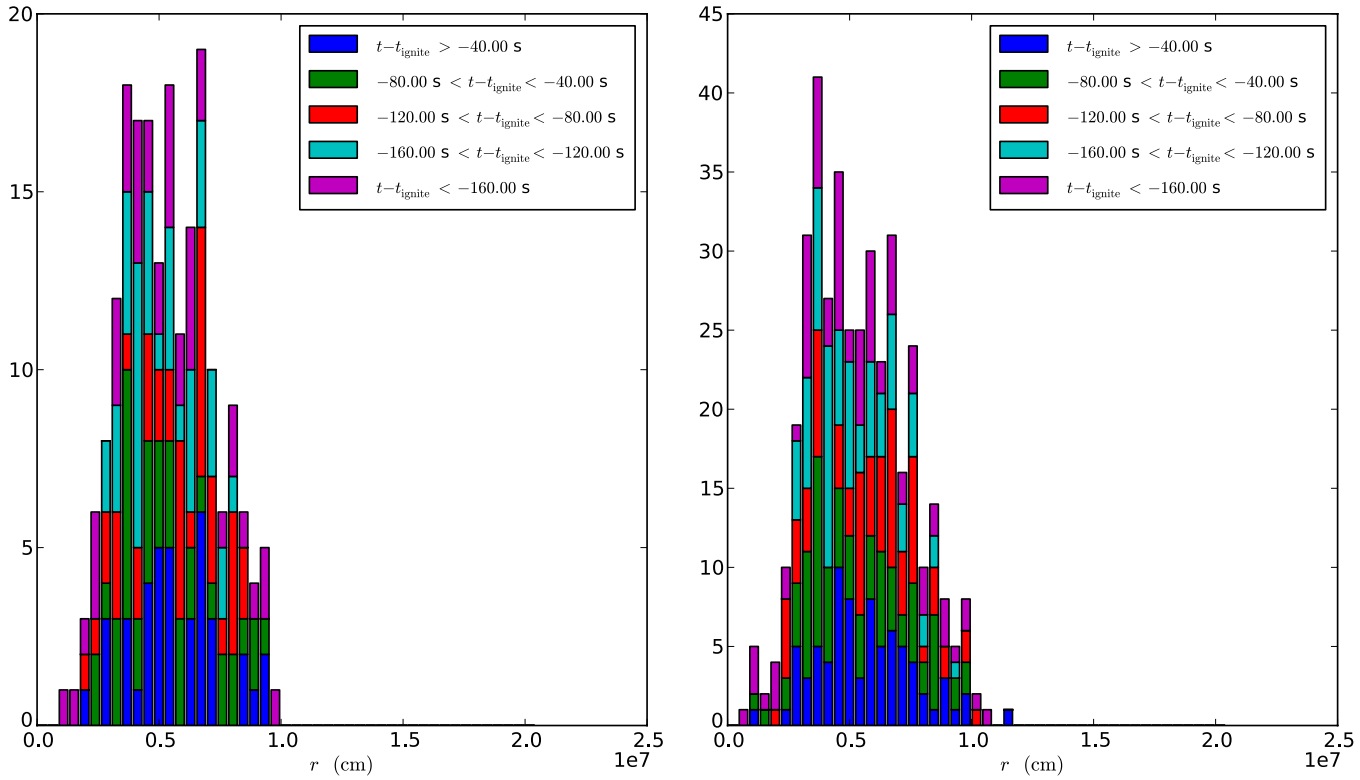

Figure 9. Histograms of the hottest cell, sorted by radius, with the colors representing time to ignition for the 4.34 km simulation with (left) $\Delta t_{\rm hist} = 1.0$ s and (right) $\Delta t_{\rm hist} = 0.5$ s.
(A color version of this figure is available in the online journal.)

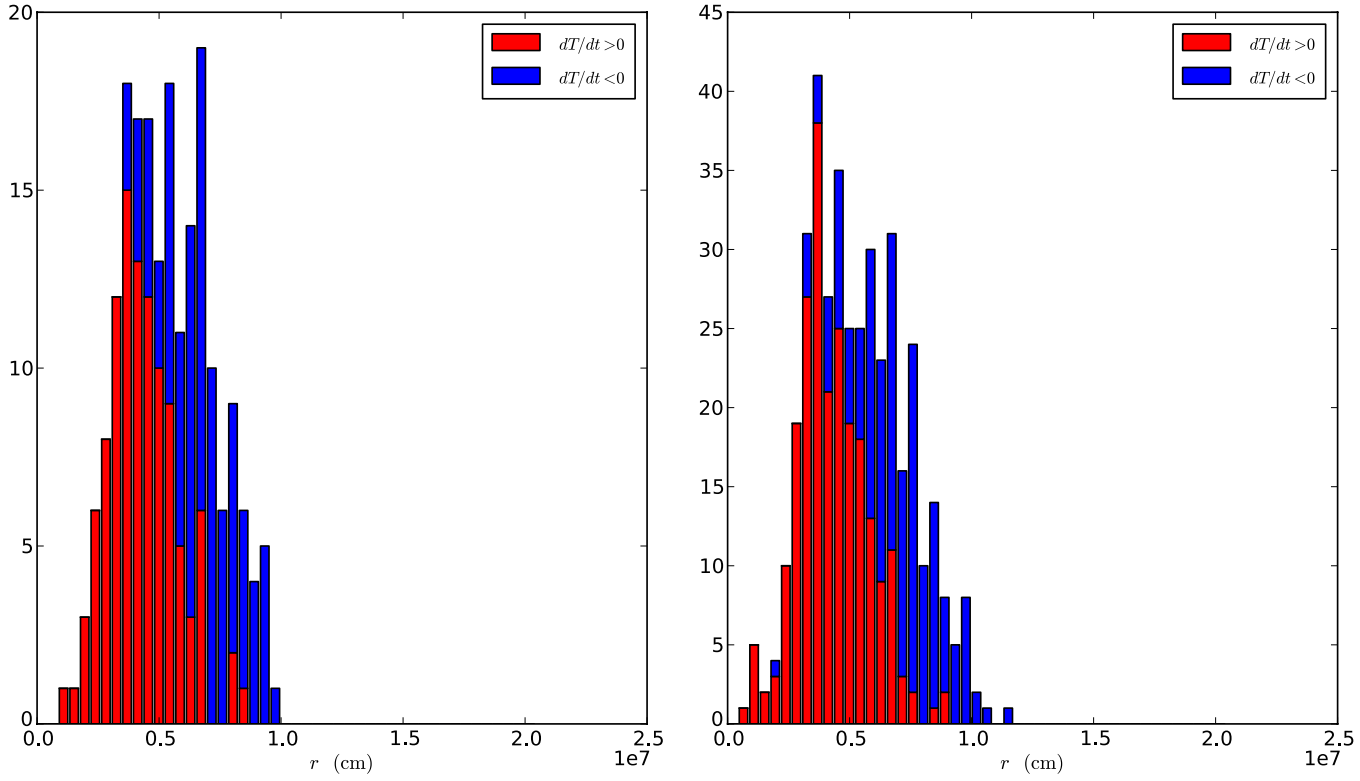

Figure 10. Histograms of the hottest cell, sorted by radius, with the colors indicating whether the temperature of the hottest cell is increasing or decreasing with time for the 4.34 km simulation with (left) $\Delta t_{\rm hist} = 1.0$ s and (right) $\Delta t_{\rm hist} = 0.5$ s.
(A color version of this figure is available in the online journal.)

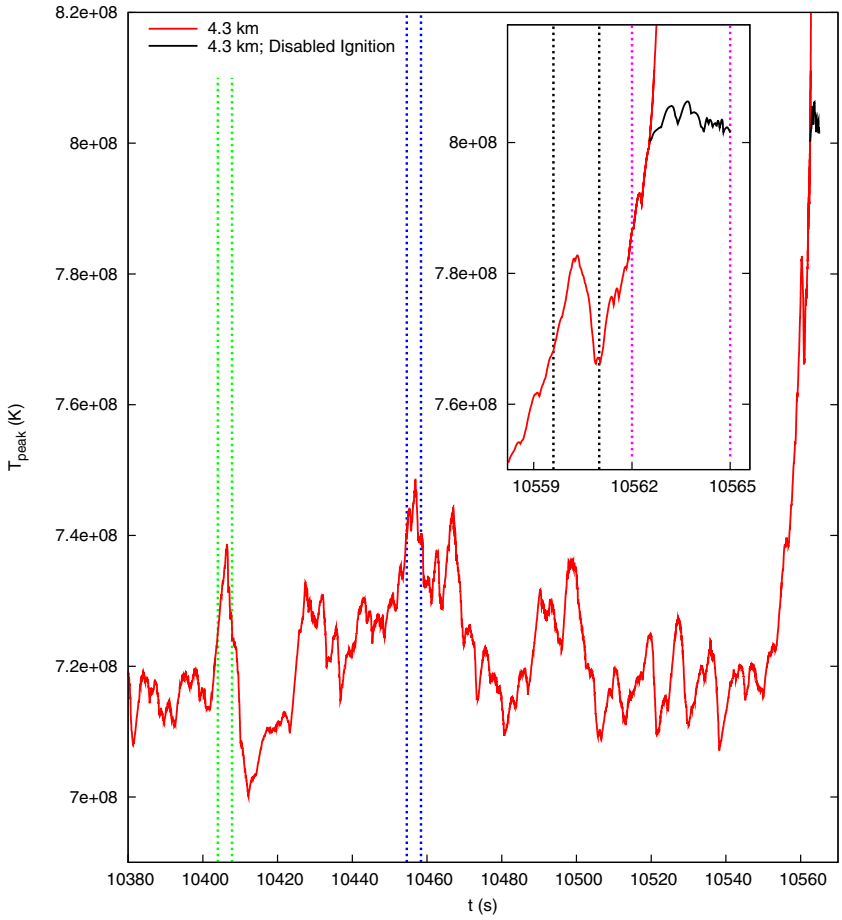

Figure 11. Peak temperature during the ∼200 s preceding ignition for the 4.34 km simulation. The dashed vertical lines indicate time ranges where we will examine whether there are multiple hot spots. The inset plot is a zoom-in of the final ∼5 s preceding ignition. The black curve follows the maximum temperature for a simulation where we disable burning in all cells with $T > 8 \times 10^8$ K.

radii to be associated with larger values of v_r as expected, since the flow will carry them away from the center.

3. In Figure 9, we see a reasonably symmetric distribution for all cases, indicating that the hot spot radius does not depend strongly on time to ignition.

Next, we include a new histogram where we examine whether the hottest cell is increasing or decreasing in temperature. Figure 10 shows histograms of the hottest cell, sorted by radius, with the colors indicating whether the temperature of the hottest cell is increasing or decreasing with time. We observe that when the hottest zone is within 40 km of the center it is almost always heating up, and when the hottest zone is outside of 75 km it is almost always cooling down. This 40–75 km range is consistent with the previous histograms. Another conclusion is that it seems highly unlikely that ignition will occur outside of 75 km since hot cells beyond that radius are most likely cooling down. This is in contrast to our result from Z11, where we claimed that 100 km was an outer limit for ignition radii.

3.3. Hot Spot Analysis

We are interested in the likelihood of multiple ignition points, so we now take a closer look at the dynamics of the last few hot spots preceding ignition. In the diagnostics we have presented, we have only been able to track the hottest cell in the simulation. We do not know, for example, if there are other hot spots elsewhere in the star that are almost as hot as the hottest zone. It is possible that at the time of ignition, there are one or more cells not directly connected to the ignition cell that have almost reached the ignition threshold. In a multiple ignition scenario, such cells could also ignite very shortly after the initial ignition. Since the white dwarf explodes within a few seconds of ignition, a multiple ignition scenario would require another ignition point to develop within the early phases of the explosion for it to have any meaningful impact. We wish to examine the temperature field very close to the ignition time to get a feel of how likely the multiple ignition scenario is.

We have previously defined a failed ignition point as a spike in the plot of the peak temperature versus time that does not run away. We begin by examining the temperature distribution in the star during three failed ignition points preceding ignition. Figure 11 is a zoom-in of Figure 3 for the final minutes preceding ignition for the 4.34 km simulation. Three failed ignition points preceding ignition are encapsulated within the green, blue, and black dotted lines. We will examine the temperature distribution in each of these time ranges to see if there are hot spots elsewhere in the star.

Figure 12 shows contours of temperature within the green dotted time region from Figure 11. We note that for all subsequent temperature visualizations, the blue dot represents the center of the star, and has a diameter of 4.34 km, corresponding to the resolution of the simulation. Also, all visualization frames are spaced at 0.2 s time intervals. The main observation is that in the frames where an orange contour exists, indicative of a hot spot, there are no other regions in the star with comparable

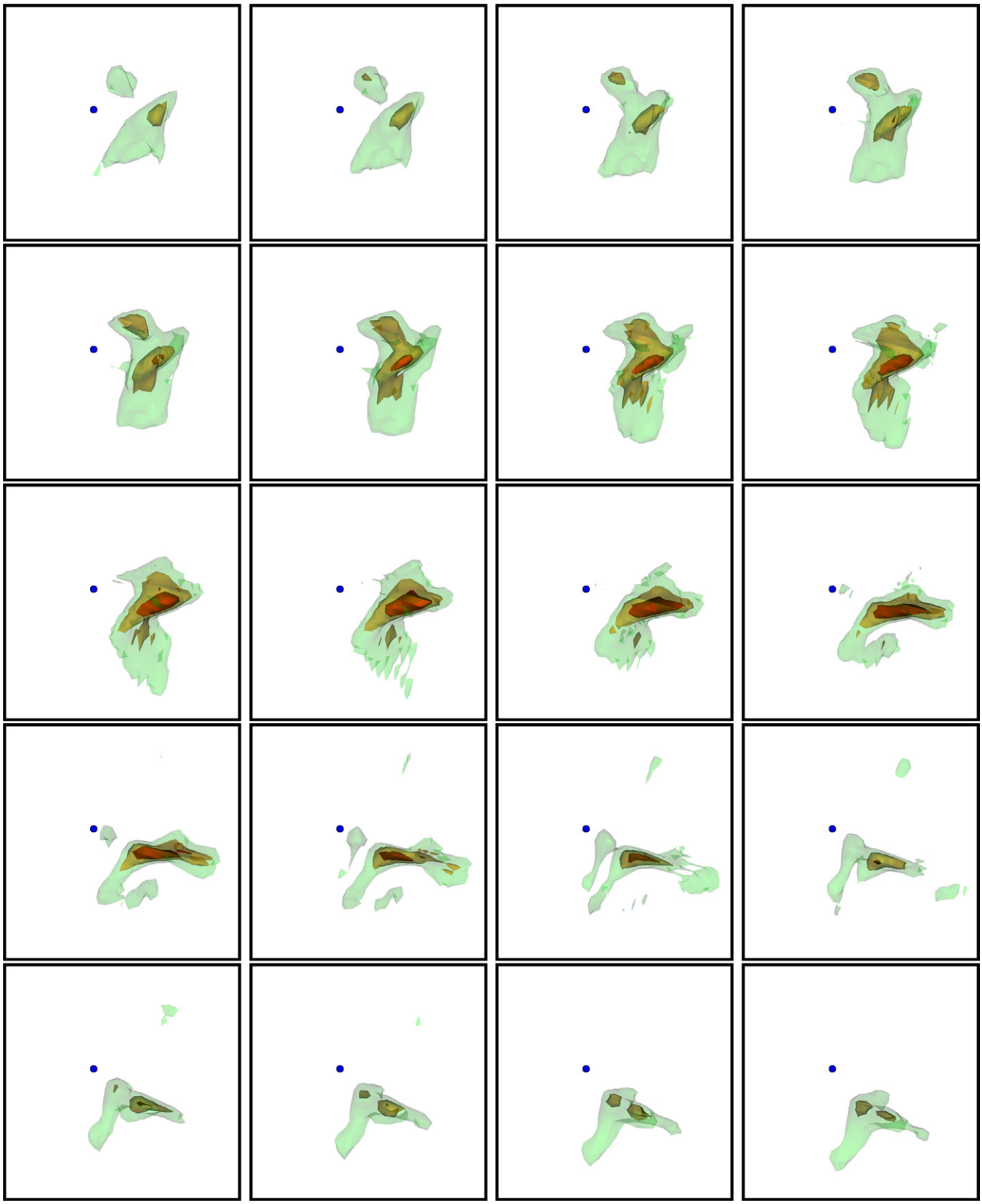

Figure 12. Temperature contours from $t = 10{,}404.0$ s to $t = 10{,}407.8$ s (corresponding to the green dotted time range in Figure 11) spaced at 0.2 s time intervals. The contours are surfaces indicating where $T = 7.15 \times 10^8$ K (green), $T = 7.2 \times 10^8$ K (yellow), and $T = 7.25 \times 10^8$ K (orange). The blue dot is at the center of the star, and has a diameter of 4.34 km, which corresponds to the grid cell width for this simulation.

(A color version of this figure is available in the online journal.)

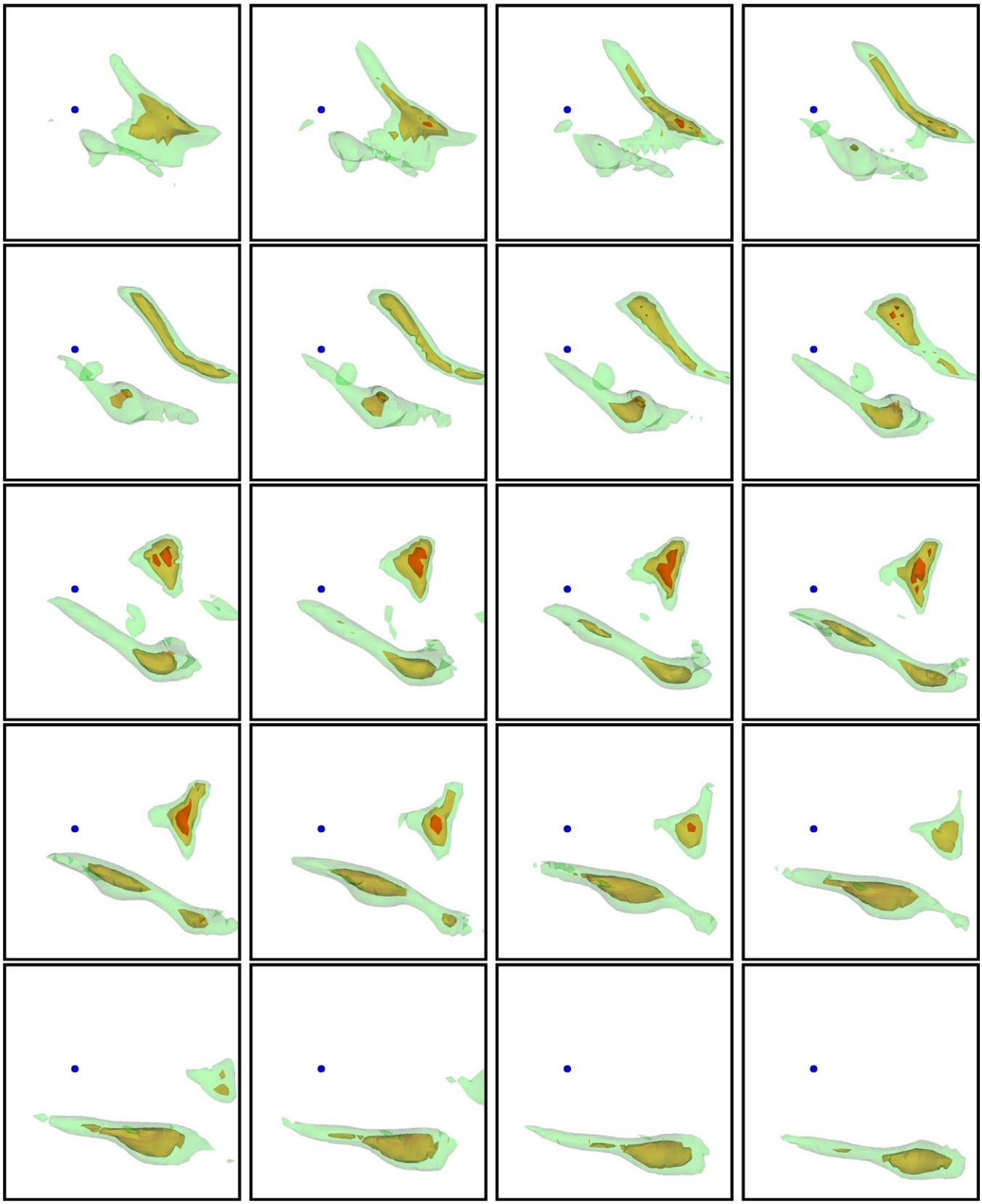

Figure 13. Temperature contours from $t = 10{,}454.6$ s to $t = 10{,}458.4$ s (corresponding to the blue dotted time range in Figure 11) spaced at 0.2 s time intervals. The contours are surfaces indicating where $T = 7.24 \times 10^8$ K (green), $T = 7.31 \times 10^8$ K (yellow), and $T = 7.38 \times 10^8$ K (orange). The blue dot is at the center of the star, and has a diameter of 4.34 km, which corresponds to the grid cell width for this simulation.

(A color version of this figure is available in the online journal.)

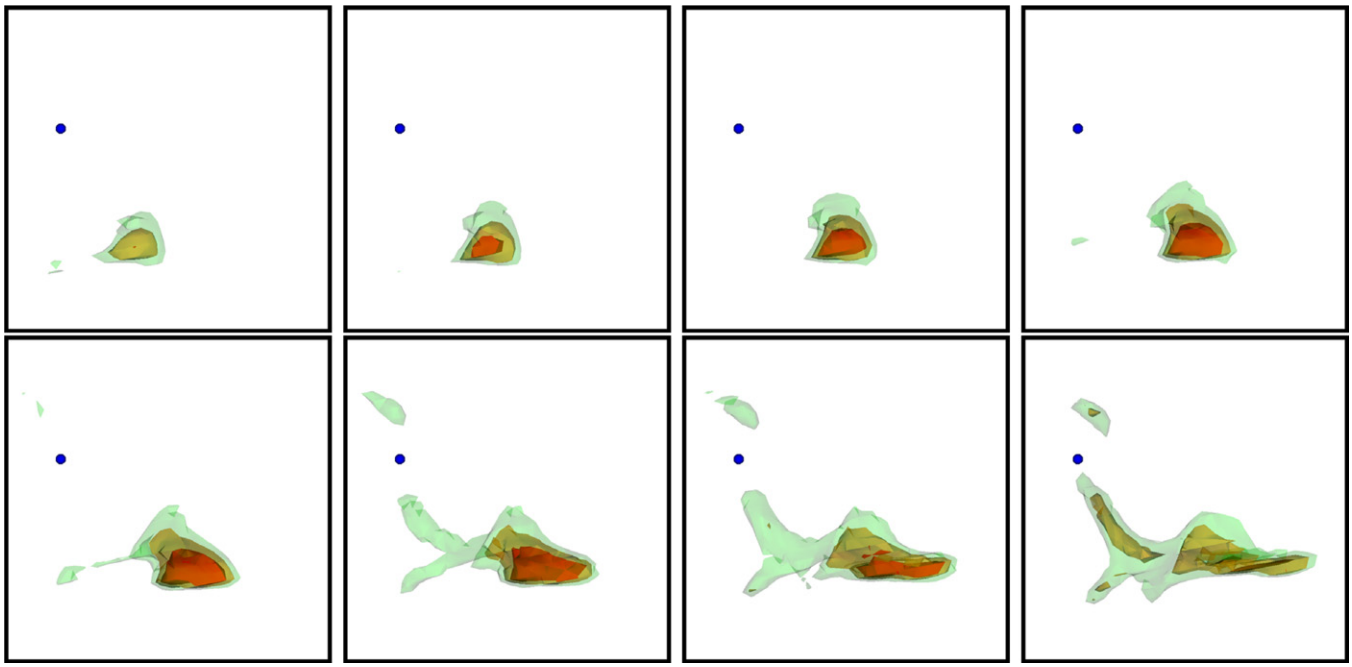

Figure 14. Temperature contours from $t = 10{,}559.2$ s to $t = 10{,}560.6$ s (corresponding to the black dotted time range in Figure 11) spaced at 0.2 s time intervals. The contours are surfaces indicating where $T = 7.48 \times 10^8$ K (green), $T = 7.54 \times 10^8$ K (yellow), and $T = 7.6 \times 10^8$ K (orange). The blue dot is at the center of the star, and has a diameter of 4.34 km, which corresponds to the grid cell width for this simulation.
(A color version of this figure is available in the online journal.)

temperature. This implies that if this hot spot were to run away, there would be only one ignition point. Figure 13 shows contours of temperature within the blue dotted time region. We do see that in the frames where an orange contour exists, there are other hot spots in different regions of the star. But as the hottest spot floats away and cools off, the temperature of the other hot spot does not increase. Again, this implies only a single ignition point. Figure 14 shows contours of temperature within the black dotted time region. This visualization is more like the green dotted time region in that there are no regions of the star with a peak temperature comparable to the main hot spot, implying that there would be only one ignition point if this hot spot were to run away.

Next, we perform another simulation, beginning at the point of ignition, in which we have disabled burning for all cells where $T > 8 \times 10^8$ K. This will give us a picture of the dynamics of nearby hot bubbles that did not initially ignite. The idea here is to let the initial ignition point float away and see if any other hot spots reach the ignition temperature soon afterward. The peak temperature in this new simulation is given by the black solid line in Figure 11. The visualization of the temperature field within the pink dotted time region from Figure 11 is shown in Figure 15. We see that the hot bubble containing the ignition cell floats away from the center of the star and cools off (because the burning is disabled) as it breaks up. More importantly, none of the other hot bubbles not connected to the ignition cell increase in temperature to the point of ignition. Altogether, our analysis of the last few hot spots does not seem to support multiple ignition points, implying that this scenario is much less likely than a single ignition point.

A caveat to this analysis is that our resolution is still several kilometers. It is possible that if one could increase the resolution far beyond what is possible today, even with AMR, then many smaller hot spots could exist and the dynamics would be different.

3.4. Convective Flow Pattern

In Z09 and Z11, we provided visualizations of the convective flow field, noting the dipole feature observed in non-rotating white dwarfs. We recall that the convectively unstable region encompasses only an inner fraction ($r \lesssim 1030$ km) of the star. Outside of this, the flow is stable against convection and dominated by large-scale structures with high circumferential velocities and a smaller radial component. Figure 16 shows visualizations of the 8.68 km, 4.34 km, and 2.17 km flow fields in the convective region at $t = 10{,}380$ s. As before, we show contours of outward and inward radial velocity, as well as contours of increasing burning rates. As expected, the burning is strongest near the center of the star. Now, we see the effect that resolution has on visualization of the velocity contours. Both the large-scale nature of the flow as well as the smaller-scale eddies are much clearer with increasing resolution. This allows us to characterize the flow field as a plume, with a small solid angle region and strong outward velocity, with a lower speed recirculation. This is in contrast to a dipole, where we would expect the magnitude of the outflow and inflow to be more similar. In Figure 17, we highlight the plume structure by showing the same 2.17 km flow field in more detail, where each frame represents a 40° rotation from the previous.

In Figure 18 we observe that, for the 4.34 km simulation at the time of ignition, the ignition point lies in a region with positive v_r (consistent with our earlier report that $v_r = 9.5$ km s^{-1}) and is almost aligned with the strongest outward plume. We expect this hot ignition point to accelerate radially outward to a significant fraction of the sound speed within a small fraction of a second; this does not give the parcel of fluid at the ignition

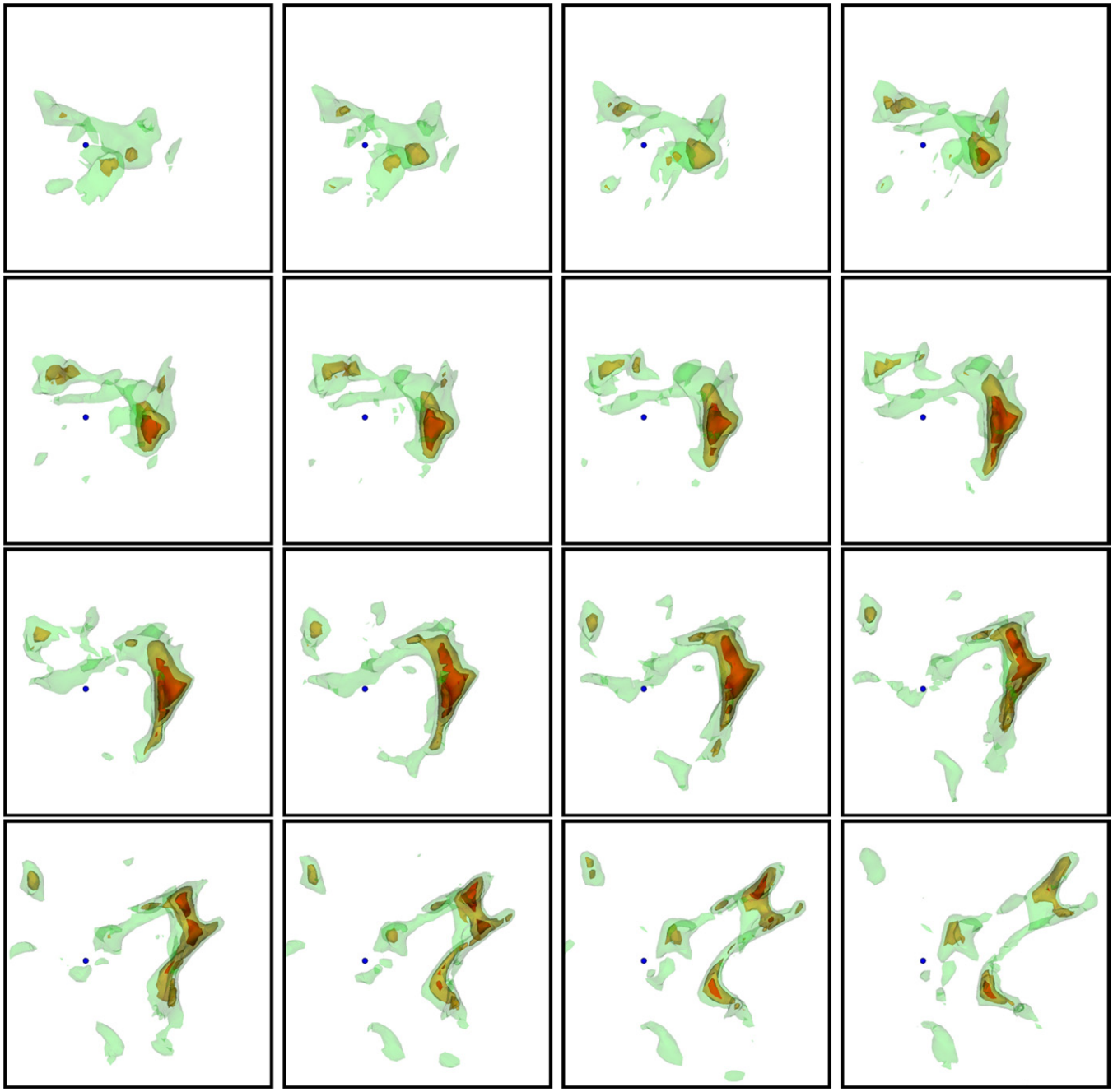

Figure 15. Temperature contours from $t = 10{,}562.0$ s to $t = 10{,}565.0$ s (corresponding to the pink dotted time range in Figure 11) spaced at 0.2 s time intervals. The contours are surfaces indicating where $T = 7.5 \times 10^8$ K (green), $T = 7.7 \times 10^8$ K (yellow), and $T = 7.9 \times 10^8$ K (orange). The blue dot is at the center of the star, and has a diameter of 4.34 km, which corresponds to the grid cell width for this simulation.

(A color version of this figure is available in the online journal.)

point enough time to change direction and align exactly with the strong outward plume.

To get an idea of the structure of the flow outside of the convective region, we visualize the flow field in the x–y plane. In Figure 19, we plot the radial velocity ($\mathbf{U} \cdot \boldsymbol{e}_r$) as well as one component of the circumferential velocity, $\mathbf{U} \cdot \boldsymbol{e}_\theta$, where $\boldsymbol{e}_\theta$ is the unit vector in the azimuthal direction in the x–y plane. Both plots use the same scale for positive and negative velocities, so we see that the circumferential velocities outside the convective region are generally larger than the radial velocities within the core. These circumferential velocities in the stably stratified region may become important in explosion simulations in that they may deform hot bubbles or flames passing through that region.

3.5. Turbulence Structure

Predictive models for SNe Ia, in particular turbulent flame models, depend critically on the structure of the turbulence in the star. In this section, we use the simulations to examine this structure and extract estimates for the turbulent intensity and the integral length scale. This will help us understand the state of the turbulence that exists at the start of the explosion phase.

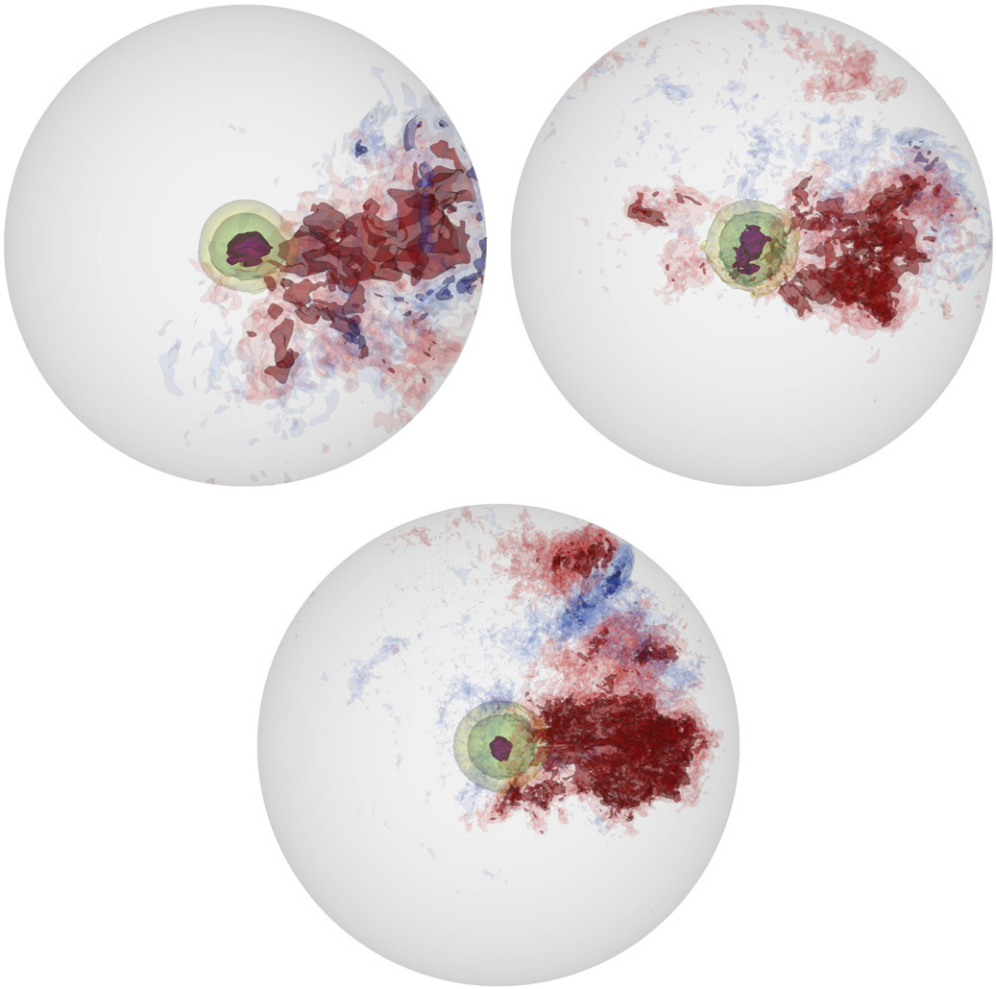

Figure 16. Contours of nuclear energy generation rate (yellow to green to purple, corresponding to 4×10^{12}, 1.27×10^{13}, and 4×10^{13} erg g^{-1} s^{-1}) and radial velocity (red is outflow, corresponding to 3×10^{6} and 6×10^{6} cm s^{-1}; blue is inflow, corresponding to -3×10^{6} and -6×10^{6} cm s^{-1}) for the (clockwise, from top left) 8.68 km, 4.34 km, and 2.17 km simulations at $t = 10{,}380$ s. Only the inner $r = 1000$ km are shown.

(A color version of this figure is available in the online journal.)

The vast majority of literature on turbulence theory deals with flows that are assumed to have constant density. In the present context, the significant variation in density due to stratification cannot be ignored and has to be dealt with carefully. Following von Weizsäcker (1951), Fleck (1983, 1996) advocated casting the energy balance equation in terms of energy density (energy per unit volume) as opposed to specific energy (energy per unit mass), and we note that the difference is inconsequential for constant density turbulence. Thus, the fundamental quantity relevant to the inertial range of a turbulent energy cascade is the energy dissipation rate per unit volume ε_V, which should be expected to scale with $\varepsilon_V \sim \rho \check{u}^3/l$, where $\check{u}$ is the turbulent intensity (rms velocity fluctuation) and l is the integral length scale. Subsequently, Kritsuk et al. (2007) used numerical simulation of compressible turbulence to demonstrate that an appropriately density-weighted velocity spectrum obeys a Kolmogorov-type five-thirds decay law. Consequently, we consider a density-weighted velocity field,

$$\mathbf{V}_n(\boldsymbol{x}) = \rho^n \mathbf{U} \quad (\mathrm{g}^n\,\mathrm{cm}^{1-3n}\,\mathrm{s}^{-1}), \tag{10}$$

and its Fourier transform,

$$\widehat{\mathbf{V}}_n(\boldsymbol{\kappa}) = \mathcal{F}[\mathbf{V}_n(\boldsymbol{x})] \quad (\mathrm{g}^n\,\mathrm{cm}^{4-3n}\,\mathrm{s}^{-1}). \tag{11}$$

We then define a generalized energy density spectrum as

$$E_n(\kappa) = \frac{1}{\Omega} \int_{\mathbf{S}(\kappa)} \frac{1}{2} \widehat{\mathbf{V}}_n(\boldsymbol{\kappa}) \cdot \widehat{\mathbf{V}}_n^*(\boldsymbol{\kappa})\, d\mathbf{S} \quad (\mathrm{g}^{2n}\,\mathrm{cm}^{3-6n}\,\mathrm{s}^{-2}), \tag{12}$$

where Ω is the volume of the domain in physical space, the domain of the integral, $\mathbf{S}(\kappa)$, is the spherical surface defined by $|\boldsymbol{\kappa}| = \kappa$, and * denotes the complex conjugate. This generalized energy density spectrum can only be made dimensionless using ε_V and κ for $n = 1/3$, resulting in the dimensionless group $\varepsilon_V^{-2/3} \kappa^{5/3} E_{1/3}(\kappa)$. Therefore, plotting $E_{1/3}(\kappa)$ should present a five-thirds decay. Henceforth, we only present energy density spectra appropriately weighted and omit the $1/3$ suffix. We also note that only $n = 1/2$ corresponds to a real energy density.

In the diagnostics in this section, we consider the local velocity, $\widetilde{\mathbf{U}}$, rather than the total velocity, $\widetilde{\mathbf{U}} + w_0 \boldsymbol{e}_r$. In Z11, we showed that the maximum magnitude of w_0 at ignition is $\sim$0.013 km s^{-1}, so the effect of w_0 is insignificant on the scales we are interested in.

Energy density spectra from the 2.17 km simulation at $t = 10{,}380$ s are shown in Figure 20(a). The density-weighted velocity field has been decomposed into different components, specifically, the Cartesian components, V_x, V_y, and V_z, and spherical polar components (using the convention that θ is

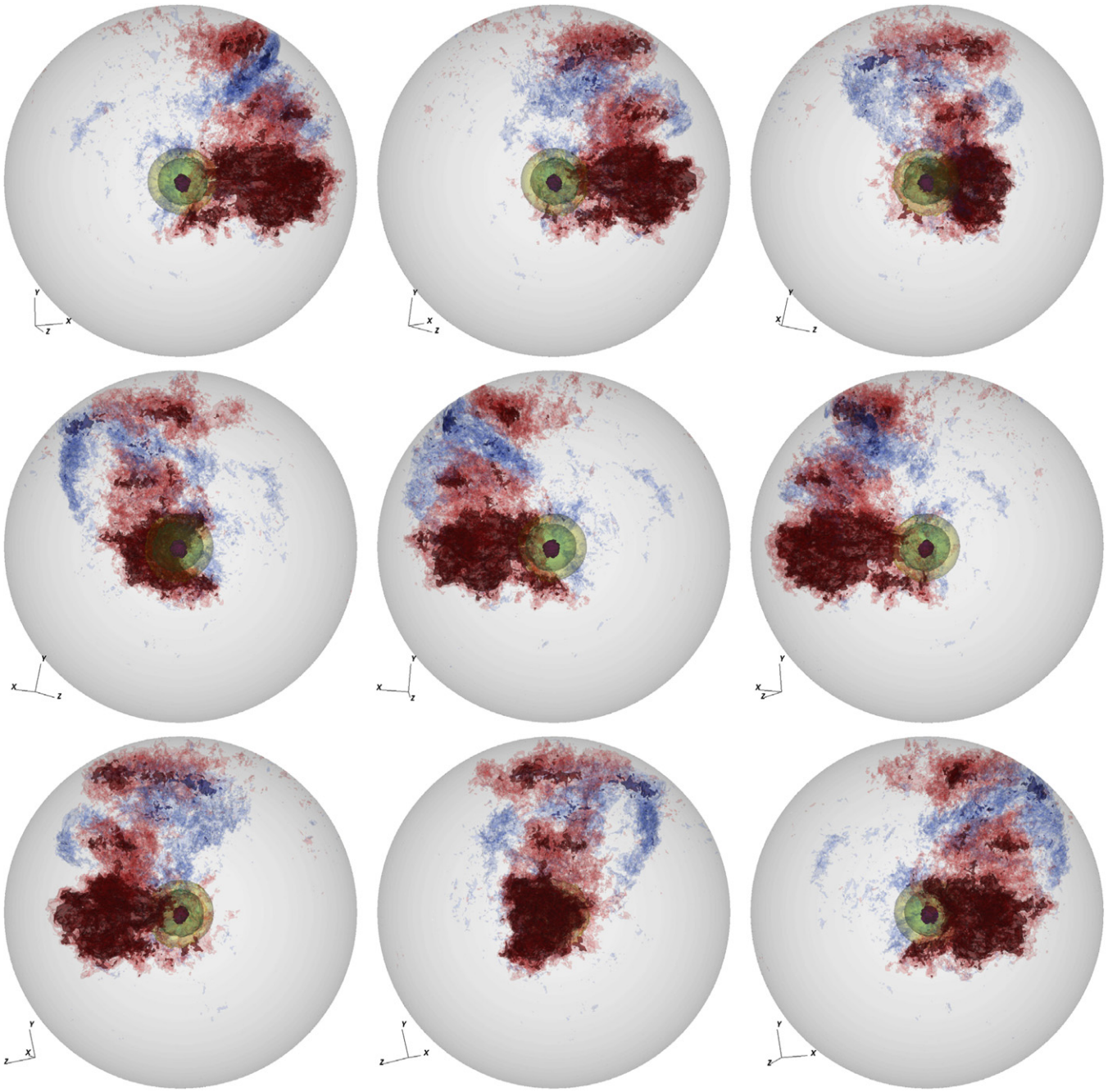

Figure 17. Same data as Figure 16, but here we only show the 2.17 km grid cell simulation and each image represents a view rotation of 40° of the data from $t =$ 10,380 s.

(A color version of this figure is available in the online journal.)

the azimuthal angle with respect to the x–y plane and φ is the inclination angle measured from the z-axis),

$$V_r = \frac{xV_x + yV_y + zV_z}{r}, \quad V_\theta = \frac{-yV_x + xV_y}{R},$$
$$V_\varphi = \frac{xzV_x + yzV_y - R^2V_z}{rR}, \tag{13}$$

where $r^2 = x^2 + y^2 + z^2$ and $R^2 = x^2 + y^2$. Three energy density spectra are plotted: first, the mean of the Cartesian components (individual components do not differ significantly from that shown); second, the radial component; and third, the circumferential component. This decomposition demonstrates that there is significantly less energy in the radial component than in the other components. This is due to the large circumferential velocities in the layers outside the convection zone; although the density is lower here, the volume is sufficiently large that the resulting energy has a significant contribution to the spectrum. It also appears that the radial component decays with an exponent close to five-thirds (if slightly smaller), and the other components have a slightly higher exponent.

To circumvent the issue of large circumferential velocities in the stably stratified region, and to remove the signal from the coarse–fine interfaces at wavenumbers around 1152 and 576, the energy density spectra of a subdomain were constructed. This was achieved by applying a smoothing function to the

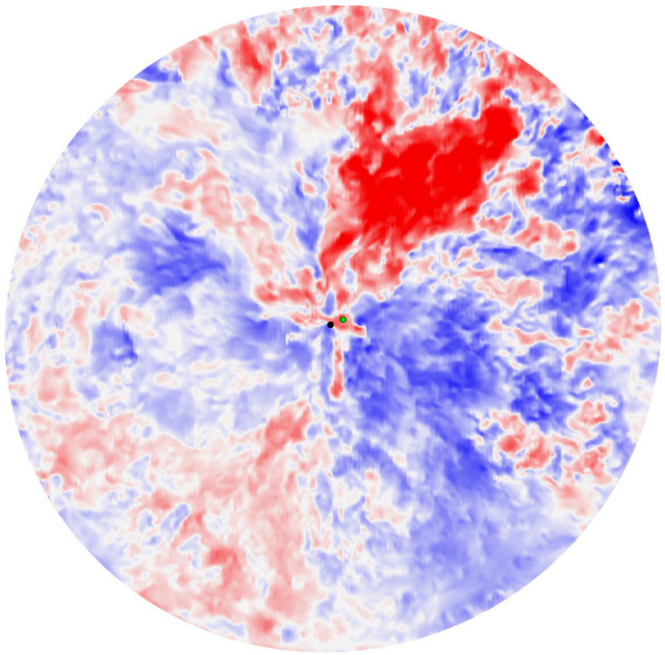

Figure 18. Planar slice from the 4.34 km simulation at the time of ignition, oriented so that the center of the star (black dot), the ignition location (green dot), and the center of the strongest outward plume lie in the plane. The dots each have a radius of 20 km. Red corresponds to $v_r > 60$ km s^{-1} and blue corresponds to $v_r < -60$ km s^{-1}. Only the inner $r = 1000$ km is shown.

(A color version of this figure is available in the online journal.)

velocity and density fields in such a way that the data outside the convection zone were set to zero. Specifically, each field was multiplied by the hyperbolic tangent function $(1 - \tanh[(r - r_0)/\delta])/2$, where $r_0 = 875$ km and $\delta = 30$ km. All of the resulting non-trivial data were at the finest AMR level, and the resulting energy density spectra are shown in Figure 20(b). Now, each spectrum collapses to a single curve, especially for $\kappa \gtrsim 20$, which corresponds to a length of about 250 km. The decay exponent of each spectrum is close to five-thirds and presents the characteristic "bump" between the inertial and dissipation ranges expected from developed homogeneous isotropic turbulence (e.g., Saddoughi & Veeravalli 1994; Porter et al. 1994; Kaneda et al. 2003; Aspden et al. 2008b).

To explore the effect of resolution on the turbulence in the convective core, Figures 20(c) and (d) present the total kinetic energy density spectra for the three resolutions, first without scaling (c), and then scaled (d). The spectra are scaled according to computational cell width and in keeping with a constant energy dissipation rate. Specifically, the 4.34 km simulation spectrum is shifted to higher wavenumbers by a factor of two, and to lower energy density by a factor of $2^{-5/3}$, and the 8.68 km spectrum has been shifted by factors of 4 and $4^{-5/3}$, respectively. The unscaled spectra demonstrate that the large scales are independent of resolution (as expected) in the sense that increasing the resolution does not lead to an increased level of turbulent intensity. This kind of convective motion is not dominated by small-scale processes, and integral quantities are well captured even at moderate resolutions. The 8.68 km simulation has a short inertial range, but this is more extensive at higher resolutions. The scaled spectra demonstrate that the dissipation range depends on the computational cell width as expected from an implicit large eddy simulation (ILES)-type simulation. In particular, there is an effective Kolmogorov length scale that is a function of the cell width; the collapse is not exact,

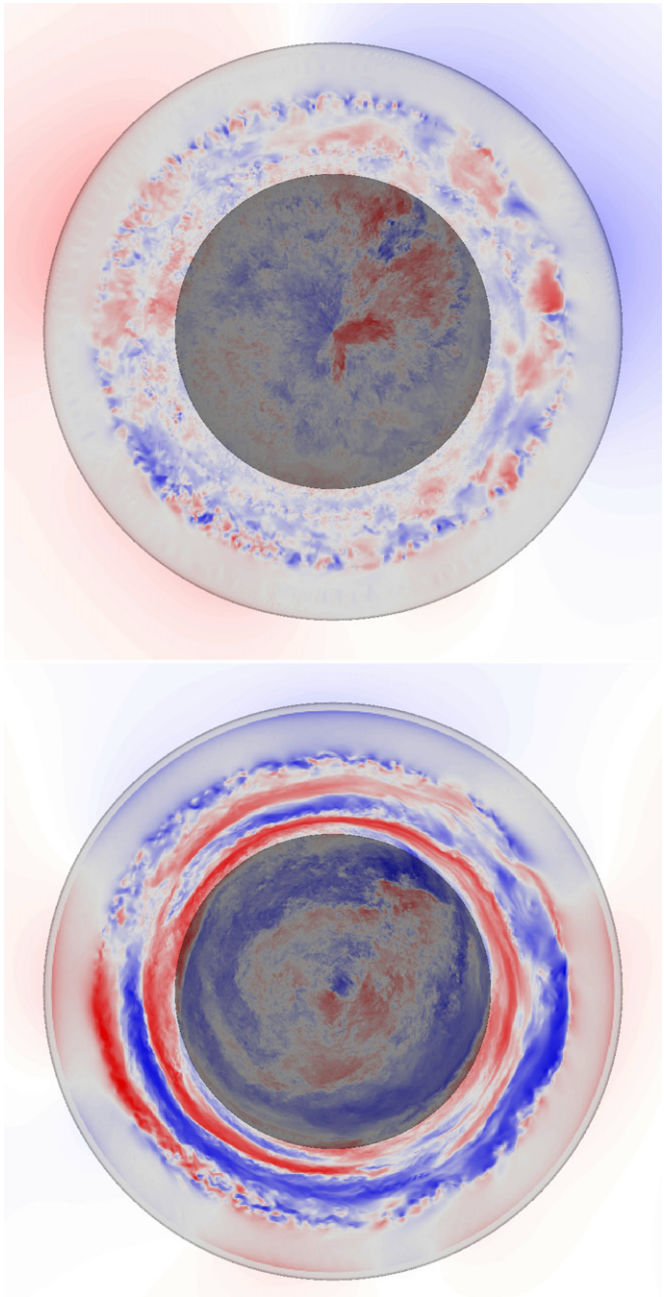

Figure 19. Top: plot of radial velocity ($\mathbf{U} \cdot \boldsymbol{e}_r$) in the x–y plane from the 2.17 km simulation at $t = 10{,}380$ s. Bottom: plot of $\mathbf{U} \cdot \boldsymbol{e}_\theta$ in the x–y plane from the same data set. In both plots, red = +100 km s^{-1} and blue = −100 km s^{-1}. The outer dark contour indicates the edge of the star, where $\rho_0 \approx 1 \times 10^5$ g cm^{-3} ($r \approx 1030$ km). The inner dark contour indicates the edge of the convective region, where $\rho_0 \approx 1.26 \times 10^8$ g cm^{-3} ($r \approx 1890$ km).

(A color version of this figure is available in the online journal.)

but is consistent with previous work (see Aspden et al. 2008b for example) which also contains further discussion of the ILES approach and dependence on resolution.

The rms velocity in the convective core ($r < 875$ km), $\breve{u}$, was found by direct measurement to be approximately 14 km s^{-1} (the data ranged from 12 km s^{-1} to 18 km s^{-1} depending on component and resolution); note that no density weighting was used. Even though this estimate is smaller than previously suggested ($\sim$100–500 km s^{-1}), we argue that it is actually an upper bound for the turbulence produced by convection because

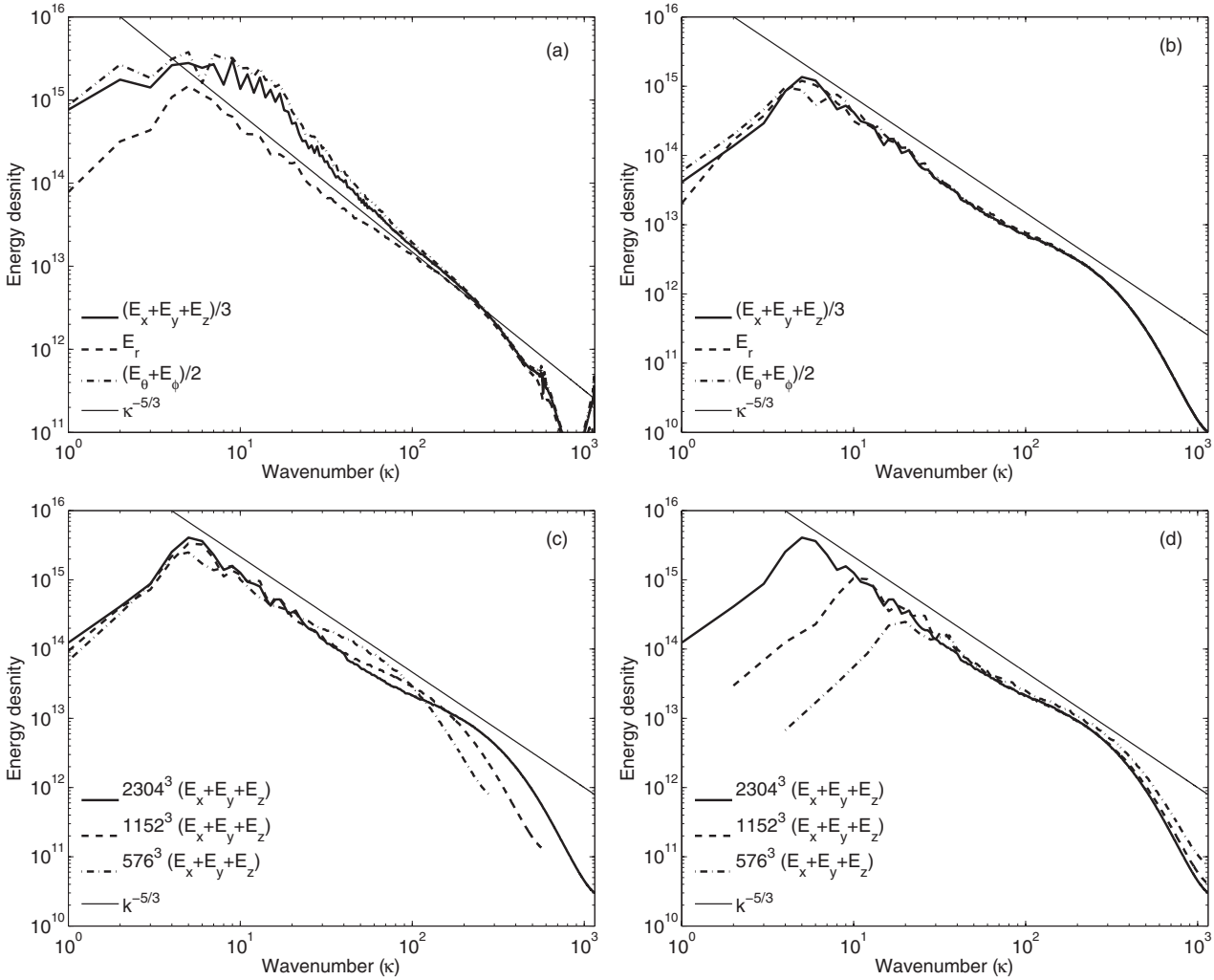

Figure 20. (a) Energy density spectra of the entire domain at 2.17 km resolution for $t = 10{,}380$ s. Note how the radial spectrum is much lower than the other components. This is due to the large circumferential velocities outside the convective core. (b) Energy density spectra for the convective core. Note how the curves have collapsed to a single profile, especially for $\kappa \gtrsim 20$, corresponding to about 250 km. (c) Comparison of the energy density spectra at the three different resolutions. (d) Same as (c), but scaled to demonstrate that the effective Kolmogorov length scale is proportional to the computational cell width.

it includes a large-scale plume-like flow, which artificially inflates the estimate.

To determine the integral length scale in the convective core, the longitudinal correlation functions were evaluated for the Cartesian components of the velocity field, along with the correlation functions of the radial velocity in each Cartesian direction, where the (second-order) velocity correlation function (two-point, one-time) is defined as

$$Q_{ij}(\boldsymbol{r}, t) = \frac{1}{\Omega} \int_{\Omega} U_i(\boldsymbol{x}, t) U_j(\boldsymbol{x} + \boldsymbol{r}, t)\, d\boldsymbol{x}, \qquad (14)$$

where $\boldsymbol{r}$ denotes the separation vector. The integral length scale in the x direction, for example, is then defined as the integral of the longitudinal velocity correlation function

$$l_x = \frac{1}{\breve{u}_x^2} \int Q_{xx}(r\boldsymbol{e}_x)\, dr. \qquad (15)$$

The correlation functions were evaluated both for the density-weighted and non-weighted velocities (by replacing U_i by V_i in Equation (14) and the appropriate normalization factor in Equation (15)) and are compared in Figure 21 by solid and dashed lines, respectively. The weighted and non-weighted

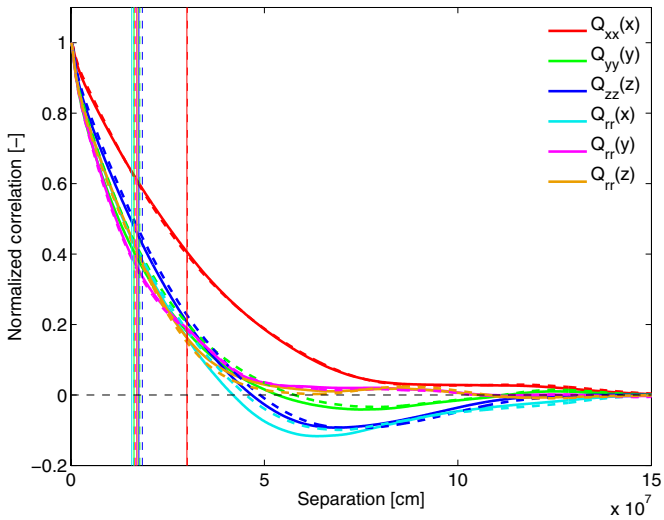

Figure 21. Longitudinal correlation functions for the turbulence in the convective core at 2.17 km resolution for $t = 10{,}380$ s. Density-weighted and non-weighted correlation functions are shown by solid and dashed lines, respectively. The x component presents a larger correlation because there is a plume-like structure roughly aligned with the x-axis. The integral length scales are denoted by the vertical lines of the corresponding color.

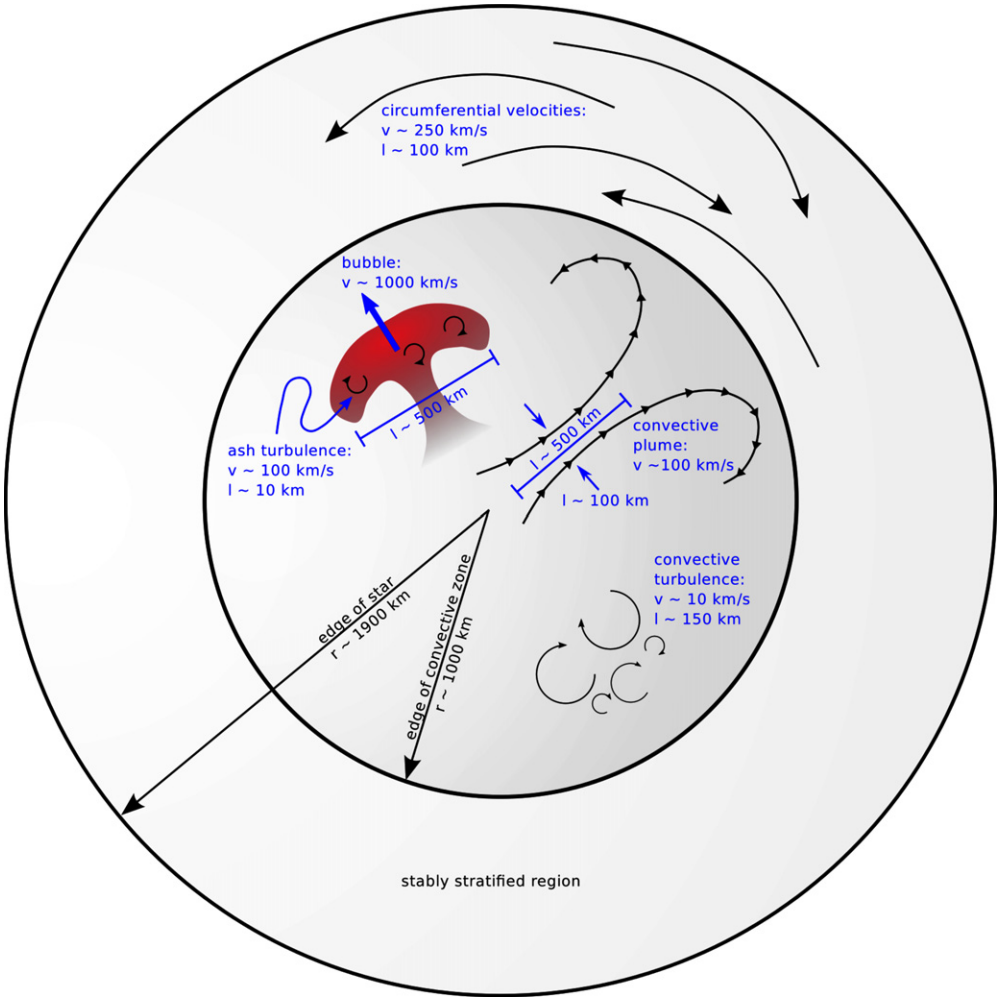

Figure 22. Schematic showing the various features with associated velocities and length scales in the white dwarf at the end of convection/start of flame propagation. (A color version of this figure is available in the online journal.)

correlation functions are in close agreement, suggesting that measuring the integral length scale is not affected by the variations in density. By integrating each correlation (ignoring the negative parts), integral length scales for each component were evaluated and are shown by the vertical lines with the corresponding line style. The x component appears to not be consistent with the other components, probably because there is a large plume-like structure roughly aligned with the x-axis. Taking this to be an outlier, the mean integral length scale was found to be approximately 169 km (with a standard deviation of approximately 8.4 km).

Averages and standard deviations of integral length scale and rms velocity were evaluated using seven time points over 350 s at the 4.34 km resolution, and were found to be approximately 200 ± 50 km and 16 ± 3 km s^{-1}, respectively.

Taking the integral length scale to be 200 km and the turbulent intensity to be 16 km s^{-1}, the specific energy dissipation rate $\varepsilon = \check{u}^3/l$ is approximately 2×10^{11} cm^2 s^{-3}. The corresponding estimates that were suggested to be necessary for a spontaneous detonation by Woosley et al. (2011) were 10 km and 500 km s^{-1}, respectively (see also Lisewski et al. 2000; Röpke et al. 2007a; Timmes & Woosley 1992). This gives $\varepsilon \sim 10^{17}$ cm^2 s^{-3}, six orders of magnitude larger. The present simulations suggest that the turbulent intensity required for a spontaneous detonation cannot be produced by convection within the core.

4. CONCLUSIONS AND DISCUSSION

Overall, our high-resolution simulations agreed with the findings of Z11 regarding the ignition radius of 50 km with a likely range of 40–75 km. We do note that the outer limit of 100 km reported in Z11 is probably too large, as we do not see any hot bubbles at that radius that are still increasing in temperature. By looking closely at the dynamics of the last few hot spots, we conclude that the multiple ignition scenario is unlikely. With improved resolution, we now describe the large-scale coherent structure in the convective field as a plume, rather than a jet, and have a better understanding of the turbulent nature of the flow.

These findings, together with those from Z11, indicate that a single-point, off-center ignition is the most likely scenario for SNe Ia. At the radii where we find ignition to be most likely, the initial flame will float away faster than it can burn toward the center (see, e.g., Plewa et al. 2004; Zingale & Dursi 2007), making for an asymmetric explosion. This scenario has been explored in explosion calculations, potentially giving rise to the "gravitationally confined detonation" (Plewa et al. 2004; Jordan et al. 2008), although other groups suggest that this mechanism

may not be robust (Röpke et al. 2007b). If a single off-center ignition fails to blow up the star, then it is possible that we would need to wait for the next ignition point, perhaps tens of seconds later, or cycle through many widely spaced ignitions until we ignite closer to the center (i.e., many successive false starts). Alternately, some type of pulsational model may ensue (Ivanova et al. 1974; Khokhlov 1991; Bravo & García-Senz 2006). With these results, the challenge to the explosion modelers is to demonstrate that the single-degenerate Chandrasekhar mass white dwarf model can produce robust explosions resulting from single-point, off-center ignition. Observations may show support for asymmetric models (Maeda et al. 2010), but some radiative transfer calculations seem to preclude extreme amounts of asymmetry (Blondin et al. 2011).

We conclude by summarizing the various components of the convecting white dwarf and give characteristic length and velocity scales for each; Figure 22 presents this information in a schematic form. Buoyancy drives a large-scale flow in the convective core, which extends to a radius on the order of 1000 km. This large-scale flow is composed of plumes around 100 km wide and several hundred km long with a bulk velocity around 100 km s^{-1}. These plumes drive turbulence in the core with an rms velocity and integral length scale that were estimated to be on the order of 16 km s^{-1} and 200 km, respectively. This level of turbulence is far below than that required for a spontaneous detonation to occur. The stably stratified region outside the convective core, extending from ∼1000 km to ∼1900 km, is made up of circumferential shear layers, with a smaller radial velocity component. These shear layers are on the order of 100 km deep, several hundred km long, with typical velocities on the order of 100 km s^{-1} and peak velocities that may be in excess of 250 km s^{-1}. The burning of a single off-center ignition would be dominated at early times by the laminar flame speed (on the order of 50 km s^{-1}) and the level of turbulence in the core is unlikely to deform the flame very much at all. Furthermore, Aspden et al. (2011) found that large-scale entrainment was the dominant process in the evolution of a burning bubble and that the flame speed (turbulent or laminar) even up to 100 km s^{-1} did not significantly affect the evolution. Therefore, the turbulence produced by convection in the core is unlikely to play a significant role in the explosion. As the bubble reaches the edge of the convective core, it will be ∼500 km across moving with a rise speed on the order of 1000 km s^{-1}. The turbulence within the bubble itself is likely to have an rms velocity on the order of 100 km s^{-1} on an integral length scale of a few tens of kilometers. In the past, it has been suggested that the convective boundary lies at the density suggested for a deflagration-to-detonation transition (Piro & Chang 2008). Although the velocities in the core are unlikely to affect the bubble as it rises, the circumferential velocities in the stable region are much greater and may interact strongly with the bubble as it passes through this region. We plan to investigate this interaction in future work.

We thank Frank Timmes for making his equation of state routines publicly available and for helpful discussions on the thermodynamics. The work at Stony Brook was supported by a DOE/Office of Nuclear Physics grant No. DE-FG02-06ER41448 to Stony Brook. The work at LBNL was supported by the SciDAC Program of the DOE Office of High Energy Physics and by the Applied Mathematics Program of the DOE Office of Advance Scientific Computing Research under U.S. Department of Energy under contract No. DE-AC02-05CH11231. The work at UCSC was supported by the DOE SciDAC program under grant No. DE-FC02-06ER41438.

Computer time for the calculations in this paper was provided through a DOE INCITE award at the Oak Ridge Leadership Computational Facility (OLCF) at Oak Ridge National Laboratory, which is supported by the Office of Science of the U.S. Department of Energy under contract No. DE-AC05-00OR22725. Visualizations were performed using the VisIt package. We thank Gunther Weber and Hank Childs for their assistance with VisIt.

REFERENCES

Almgren, A., Bell, J., Kasen, D., et al. 2010, in Proc. SciDAC 2010, http://computing.ornl.gov/workshops/scidac2010/papers.shtml
Almgren, A. S., Beckner, V. E., Bell, J. B., et al. 2010, ApJ, 715, 1221
Almgren, A. S., Bell, J. B., Colella, P., Howell, L. H., & Welcome, M. 1998, J. Comput. Phys., 142, 1
Almgren, A. S., Bell, J. B., Nonaka, A., & Zingale, M. 2008, ApJ, 684, 449
Almgren, A. S., Bell, J. B., Rendleman, C. A., & Zingale, M. 2006a, ApJ, 637, 922
Almgren, A. S., Bell, J. B., Rendleman, C. A., & Zingale, M. 2006b, ApJ, 649, 927
Aspden, A. J., Bell, J. B., Day, M. S., Woosley, S. E., & Zingale, M. 2008a, ApJ, 689, 1173
Aspden, A. J., Bell, J. B., Dong, S., & Woosley, S. E. 2011, ApJ, 738, 94
Aspden, A. J., Bell, J. B., & Woosley, S. E. 2010, ApJ, 710, 1654
Aspden, A. J., Bell, J. B., & Woosley, S. E. 2011, ApJ, 730, 144
Aspden, A. J., Nikiforakis, N., Dalziel, S. B., & Bell, J. B. 2008b, Commun. Appl. Math. Comput. Sci., 3, 103
Berger, M. J., & Colella, P. 1989, J. Comput. Phys., 82, 64
Blondin, S., Kasen, D., Roepke, F. K., Kirshner, R. P., & Mandel, K. S. 2011, MNRAS, 417, 1280
Bravo, E., & García-Senz, D. 2006, ApJ, 642, L157
Brown, P. N., Byrne, G. D., & Hindmarsh, A. C. 1989, SIAM J. Sci. Stat. Comput., 10, 1038
Bychkov, V. V., & Liberman, M. A. 1995, A&A, 304, 440
Day, M. S., & Bell, J. B. 2000, Combust. Theory Modelling, 4, 535
Fleck, R. C., Jr. 1983, ApJ, 272, L45
Fleck, R. C., Jr. 1996, ApJ, 458, 739
García-Senz, D., & Bravo, E. 2005, A&A, 430, 585
Garcia-Senz, D., & Woosley, S. E. 1995, ApJ, 454, 895
Höflich, P., & Stein, J. 2002, ApJ, 568, 779
Iapichino, L., Brüggen, M., Hillebrandt, W., & Niemeyer, J. C. 2006, A&A, 450, 655
Iapichino, L., & Lesaffre, P. 2010, A&A, 512, A27
Ivanova, L. N., Imshennik, V. S., & Chechetkin, V. M. 1974, Ap&SS, 31, 497
Jordan, G. C., IV, Fisher, R. T., Townsley, D. M., et al. 2008, ApJ, 681, 1448
Kaneda, Y., Ishihara, T., Yokokawa, M., Itakura, K., & Uno, A. 2003, Phys. Fluids, 15, L21
Khokhlov, A. M. 1991, A&A, 245, L25
Khokhlov, A. M. 1995, ApJ, 449, 695
Khokhlov, A. M., Oran, E. S., & Wheeler, J. C. 1997, ApJ, 478, 678
Kritsuk, A. G., Norman, M. L., Padoan, P., & Wagner, R. 2007, ApJ, 665, 416
Kuhlen, M., Woosley, S. E., & Glatzmaier, G. A. 2006, ApJ, 640, 407
Lisewski, A. M., Hillebrandt, W., Woosley, S. E., Niemeyer, J. C., & Kerstein, A. R. 2000, ApJ, 537, 405
Livne, E. 1993, ApJ, 406, L17
Livne, E., Asida, S. M., & Höflich, P. 2005, ApJ, 632, 443
Ma, H. 2011, PhD thesis, Univ. California, Santa Cruz
Maeda, K., Benetti, S., Stritzinger, M., et al. 2010, Nature, 466, 82
Mueller, E., & Arnett, W. D. 1986, ApJ, 307, 619
Niemeyer, J. C., & Hillebrandt, W. 1995, ApJ, 452, 769
Niemeyer, J. C., Hillebrandt, W., & Woosley, S. E. 1996, ApJ, 471, 903
Niemeyer, J. C., & Woosley, S. E. 1997, ApJ, 475, 740
Nomoto, K., Thielemann, F.-K., & Yokoi, K. 1984, ApJ, 286, 644
Nonaka, A., Almgren, A. S., Bell, J. B., et al. 2010, ApJS, 188, 358
Nonaka, A., Almgren, A. S., Bell, J. B., et al. 2011, in Proc. SciDAC 2011, in press
Pan, L., Wheeler, J. C., & Scalo, J. 2008, ApJ, 681, 470
Pember, R. B., Howell, L. H., Bell, J. B., et al. 1998, Comb. Sci. Tech., 140, 123
Piro, A. L., & Chang, P. 2008, ApJ, 678, 1158
Plewa, T., Calder, A. C., & Lamb, D. Q. 2004, ApJ, 612, L37

Porter, D. H., Pouquet, A., & Woodward, P. R. 1994, Phys. Fluids, 6, 2133
Rendleman, C. A., Beckner, V. E., Lijewski, M., Crutchfield, W. Y., & Bell, J. B. 2000, Comput. Vis. Sci., 3, 147
Röpke, F. K., Hillebrandt, W., & Niemeyer, J. C. 2004, A&A, 421, 783
Röpke, F. K., Hillebrandt, W., Schmidt, W., et al. 2007a, ApJ, 668, 1132
Röpke, F. K., Woosley, S. E., & Hillebrandt, W. 2007b, ApJ, 660, 1344
Saddoughi, S. G., & Veeravalli, S. V. 1994, J. Fluid Mech., 268, 333
Timmes, F. X., & Woosley, S. E. 1992, ApJ, 396, 649
von Weizsäcker, C. F. 1951, ApJ, 114, 165
Woosley, S. E., Almgren, A., Bell, J. B., et al. 2007, J. Phys.: Conf. Ser., 78, 012081
Woosley, S. E., Kerstein, A. R., & Aspden, A. J. 2011, ApJ, 734, 37
Woosley, S. E., Kerstein, A. R., Sankaran, V., Aspden, A. J., & Röpke, F. K. 2009, ApJ, 704, 255
Zingale, M., Almgren, A. S., Bell, J. B., Nonaka, A., & Woosley, S. E. 2009, ApJ, 704, 196
Zingale, M., & Dursi, L. J. 2007, ApJ, 656, 333
Zingale, M., Nonaka, A., Almgren, A. S., et al. 2011, ApJ, 740, 8